COMPUTATIONAL ANALYSIS OF SHAPE MEMORY ALLOY SENSORY PARTICLES FOR STRUCTURAL HEALTH MONITORING APPLICATIONS

A Thesis

by

BRENT RYAN BIELEFELDT

Submitted to the Office of Graduate and Professional Studies of
Texas A&M University
in partial fulfillment of the requirements for the degree of

MASTER OF SCIENCE

Chair of Committee,	Amine Benzerga
Co-Chair of Committee,	Darren Hartl
Committee Members,	Alan Needleman
	Ibrahim Karaman
Head of Department,	Rodney Bowersox

August 2016

Major Subject: Aerospace Engineering

ABSTRACT

The development of new structural damage detection methods is of great interest to the aerospace industry. Current detection techniques rely on experiences with similar vehicles operating in similar conditions and require disassembly and part-by-part inspection. While effective, these methods can be costly, inefficient, and unnecessary if the aircraft is not in danger of structural failure. It is imagined that future aircraft will utilize non-destructive evaluation methods, allowing for the near real-time monitoring of structural integrity. A particularly interesting method involves utilizing the unique transformation response of shape memory alloy (SMA) particles embedded in an aircraft structure. By detecting changes in the mechanical and/or electromagnetic responses of embedded particles, operators could detect the formation or propagation of fatigue cracks in the vicinity of these particles.

This work seeks to demonstrate the ability of SMA sensory particles to detect structural damage using a computational approach. For the first time, sensory particle response to local damage is demonstrated using finite element modeling. This model, based on an experimental demonstration, allows for the determination of sensory particle material properties by matching experimental data to finite element simulations. The result is then used to predict particle response to a propagating crack in the root rib of an aircraft wing using finite element analysis. In particular, this model utilizes substructure modeling to maintain computational efficiency while relating globally applied loads to local structural response. Finally, this work examines whether sensory particles can be used to approximate the location of structural damage by interpolating a stress field based on the responses of sensory particles in the vicinity of a propagating crack.

DEDICATION

To CEB and DJB,
for instilling in me a sense of
curiosity about the world.

"The very existance of aviation is proof that man, given the will, has the capacity to accomplish deeds that seem impossible."

-*Eddie Rickenbacker*

ACKNOWLEDGEMENTS

I would be remiss if I did not first thank God for blessing me with His gifts and continually creating opportunities for me to do what I love. May this work and all future works serve to glorify Your name.

There are not enough pages in the world for me to adequately thank my Mom and Dad for the love and support they've given me. They are the perfect team: Mom (lovingly) keeping me grounded and pushing me academically, and Dad keeping things light and reminding me to not take myself so seriously. The transition from undergraduate life in Tuscaloosa to graduate life in College Station has not been an easy one, but they have encouraged me every step of the way. Above all, they have taught me the virtues of hard work and dedication, and that all you can do is your best. I could not ask for better parents.

I would also like to thank my girlfriend and best friend Jessica for the incredible amount of encouragement she has given me over the past 2 years. She has experienced every high and low along with me, and has done so with a smile. She has taken 1 AM phone calls when codes aren't working right and 2AM phone calls when I've found the error, proofread papers, and listened to dozens and dozens of presentation practices. Her ability to always make me laugh has made productive days great and frustrating days better. I am so thankful for her.

This work would not have been possible without the direction I've received from my advisor, Dr. Darren Hartl. From being patient with me as I came to Texas A&M and took a crash course in Python and Abaqus, to teaching me how to balance being a researcher and a student, he has truly been a great mentor. He took my interests into account and developed ideas to incorporate them into my work. His expecta-

tions have pushed me further than I ever thought I could go, and I have become a better engineer for it. I look forward to working with him in the future.

I would like to thank the members of my committee for their input on this thesis. Dr. Amine Benzerga gave me my first rigorous introduction to continuum mechanics, and has been a great resource on the theory behind damage and failure in materials. Interacting with Dr. Ibrahim Karaman has helped me change my perspective to consider not only the applications of my work, but the underlying material science behind them. I would also like to thank Dr. Alan Needleman for his contributions, as well as Dr. Patrick Shamberger for providing input during my thesis defense and helping me close some loose ends in this work.

Of course, this work has not strictly been a Texas A&M effort. I would like to thank Dr. Jacob Hochhalter, Dr. Paul Leser, and the rest of the Damage Tolerance and Reliability Branch at the NASA Langley Research Center for their help on this project and for hosting me for a summer. They gave me my first exposure to a professional research environment, and their help with understanding and implementing the damage model was crucial to the completion of this project.

My research has also benefited from the interactions I've had with my fellow students. Chris Bertagne has been a great sounding board for me, and has always been willing to help me with any programming-related questions I stumble upon. Edwin Peraza-Hernandez has been a wealth of knowledge when working with Abaqus and the UMAT, and somehow finds time to help us all with our research while simultaneously doing his own. Will Scholten and Ryan Patterson have made working in the basement entertaining, and Nick Barta's help in understanding the material science behind my work has been greatly appreciated.

Thank you all.

TABLE OF CONTENTS

Page

LIST OF FIGURES

FIGURE Page

LIST OF TABLES

TABLE Page

1. INTRODUCTION

1.1 Motivation

Since its development by the Wright brothers in 1903, the airplane has become a fixture in our society. Its various applications, from commercial to military, have made it an essential part of various industries. As such, it has become the subject of intensive research in hopes of improving its performance and thus expanding its mission envelope. While technological advances have markedly increased capability, it has also led to the operation of aircraft in harsh operating conditions for extended periods of time. These aircraft may experience unforeseen loading that is difficult to reproduce during ground testing. Additionally, research in materials science has led to the implementation of complex materials in aircraft; while helping to increase performance, these materials' responses to the previously mentioned loading may be difficult to predict. These issues have made detecting structural defects prior to operation of paramount importance.

Traditional damage detection techniques fall under the category of *time-based maintenance* [21]. Aircraft currently undergo routinely scheduled inspections to ensure they can maintain structural integrity during operational loading [23]. This involves a vehicle being removed from service, disassembled, and inspected part-by-part, with repairs taking place on an as-needed basis [64]. This method has proven effective; just 4% of aircraft hull loss found to have been caused by structural deficiencies [4]. However, this remains a costly process due to both labor costs as well as loss of production volume [5]. Other complications, such as improper reassembly of the vehicle or inadvertent damage during repairs, can also arise. Furthermore, this method is noticeably inefficient. Inspections are scheduled based on operators' expe-

riences with similar aircraft operating in similar conditions. Given that each vehicle is unique, it is possible that an aircraft that is in little to no danger of structural failure could be unnecessarily removed from operation and inspected. Additionally, close to 90% of all aircraft inspections are strictly visual [60], meaning that a significant amount of structural damage can occur inside a component without being detected. This method is further hindered by its inability to provide real-time updates as to the structural integrity of the vehicle; this is a key issue for spacecraft, which operate for long periods of time without being inspected.

Far more efficient methods for structural health monitoring use *condition-based maintenance*, where an aircraft is removed from service and repaired only when it is in danger of structural failure. In particular, the increased use of smart materials in aerospace applications has led to the proposal of *smart monitoring systems* which can provide a near real-time understanding of the structural integrity of an aircraft [21]. These systems could utilize non-destructive evaluation (NDE) methods and would have the advantage of being unique to each aircraft, and the information generated by these systems can help influence operation to maximize vehicle lifetime [69]. These methods are also far more time-efficient, with the use of smart monitoring systems estimated to reduce the inspection time of a fighter jet by 44% [5].

1.2 Literature Review of NDE Methods

In the aerospace industry, two methods have already been explored and show great promise: ultrasonic testing and eddy current testing [10]. The following sections provide a brief review of these two methods, as well as other popular methods that may be applicable to the aerospace industry in the future.

1.2.1 Ultrasonic Method

Nondestructive testing can be carried out using sound waves above the audible range ($\sim$20 Hz). Driven by high voltage electrical pulses, a piezoelectric or electromagnetic transducer generates high frequency ultrasonic energy. This energy is introduced into the material and propagates in the form of waves. The presence of a discontinuity in the material (i.e. structural damage) results in some waves reflecting off the surface of the flaw and back to the transducer. The reflected wave signal is then transformed into an electrical signal by the transducer and is displayed on a screen. From this signal, the discontinuity location, as well as its size and orientation can be determined [42, 9, 7, 39]. Ultrasonic testing has been shown to have superior depth of penetration for flaw detection compared to other methods. It also requires minimal part preparation and can provide instantaneous results when using appropriate electronic equipment. However, ultrasonic testing requires the surface of the component in question to be accessible and usually requires a coupling medium to facilitate the transfer of sound waves into the specimen. This method has also been found to be unreliable when inspecting components that are rough, exceptionally thin, heterogeneous, or contain complex geometries [42]. Additionally, ultrasonic testing is difficult when considering course-grained materials due to low sound transmission and high signal noise [42]. Finally, linear defects oriented parallel to the sound waves may go undetected.

There are numerous examples of the use of ultrasonic testing in aerospace applications. Work done by Matt et al. studied the possibilty of using an ultrasonic method to monitor skin-to-spar bonded joints in unmanned arial vehicles (UAVs) [44]. Mueller et al. detailed the use of ultrasonic testing to reveal bond defects between titanium stepped-up joints and composite surfaces in tactical aircraft wings

[47]. This method has also shown to be effective in space applications, such as evaluating bolted connections in satellites as shown by Montoya et al [46]. Recently, the use of optical fibers in combination with ultrasonic testing has received attention for applications where electromagnetic interference needs to be avoided or where additional parameters also need to be monitored (i.e. strain or temperature) [10]. Sun et al. developed an optical fiber-guided robotic laser ultrasonic system for use in the inspection of composite structures [67]. Betz et al. combined Lamb wave-detecting fiber Bragg grating in optical fibers genetic algorithms to achieve good results in approximating the location of holes in metallic aerospace materials [8]. Work done by Straszerski et al. used a similar method to detect impact damage in an aircraft wing [65].

1.2.2 Eddy Current Method

A second NDE method uses the principles of electromagnetism to detect structural damage. When an alternating current is applied to a conductive probe, a dynamic expanding and contracting magnetic field develops around the probe. When a second conductive material (the component being detected) is placed in the vicinity of this dynamic magnetic field, eddy currents, or currents that flow in a circular path, are induced in the material. These eddy currents generate their own (secondary) magnetic field which opposes the (primary) magnetic field generated by the probe. This weakening of the primary magnetic field results in a change in the impedance of the probe. The presence of structural defects in the material obstructs the flow of eddy currents, which reduces the secondary magnetic field and increases probe impedance. These changes in impedance can be detected, amplified, and displayed [45, 42, 74, 63]. Eddy current testing requires minimal part preparation, can be used without contacting the part in question, and works well with complex geometries.

However, this method works only with conductive materials and offers limited depth of penetration. Eddy current testing also requires access to the surface of the component and can miss structural defects that lie parallel to the probe. Additionally, eddy current sensors have strict calibartion requirements due to large sensor variability. It has been found that nominally identical eddy current probes can produce signals that differ by up to 35% [2].

Eddy current testing has been the subject of research for aerospace applications. Rao and Nakagawa investigated the effect of various materials and probes on eddy current testing and established baselines for various types of structural defects for the development of a model-based approach to inspection [57]. This model reaches good agreement with experimental data and could potentially substitute for laborious experimental investigations. Sodano developed an automated eddy current sensor to detect structural defects in aircraft components [63]. This sensor showed a variation in impedance when in the vicinity of both corrosion and a small hole. Studies performed by Washabaugh et al. cover the applications of shaped-field eddy current Meandering Winding Magnetometer (MWM) sensors and MWM arrays [74]. One such application allows for MWM arrays to be mounted or embedded in aircraft components to detect the formation of cracks. However, these sensors are not capable of sensing damage outside of the footprint of the sensor; as such, sensors must either be strategically placed in areas where cracks are predicted to form or more sensors are required to monitor the entire structure. A second application involves scanning for corrosion on the inaccessible backside of plates on a C-130 flight deck using MWM arrays.

1.2.3 Other NDE Methods

Radiography can also be used to locate hidden structural defects in aircraft structures such as cracking and corrosion. This method has been implemented by the Air Force at McClellan Air Force Base, where a robotic real-time radiography system can rapidly inspect large sections of aircraft [12]. Additionally, the Air Force Research Lab developed a smaller and mobile semiautomated system using high resolution real-time radiography (HRRTR) capabilities, which decreased inspection time by an estimated factor of at least three [22]. This system has been used to detect structural damage (both cracking and corrosion) on Boeing 707 lap joints and fuselage-deck joints [12].

Another damage detection method found extensively in the literature is vibration-based NDE. This method takes advantage of the idea that structural damage alters the stiffness, mass or energy dissipation properties of a system; these changes are noticable when compared with the original response of a pristine structure. This method can be challenging given that damage is often a localized phenomenon and may not significantly influence the global structural response [20]. While vibration-based damage detection has been used primarily for monitoring rotating machinery, it has found its uses in aerospace applications. NASA began utilizing vibration-based inspection in conjunction with the development of the Space Shuttle. The Shuttle Modal Inspection System (SMIS) was developed to identify structural damage in control surfaces, lifting surfaces, and fuselage panels [27, 20]. These components were covered with a thermal protection system, making them inaccessible to other NDE methods. All orbital vehicles have been subjected to SMIS testing since 1987.

Liquid penetrant inspection is a method that uses colored dye to reveal surface breaking flaws. This is based on the ability of a liquid to be drawn into a disconti-

nuity via capillary action. After excess penetrant is removed from the surface of a component, a developer acts to draw the penetrant from the surface flaw to reveal its presence. Liquid penetrants have often been used as an intial inspection method for weldments in the aerospace industry[76].

1.3 Sensory Particle NDE Method

Recently, an NDE method was developed that could allow for the real-time monitoring of structural damage [73, 40, 15]. By embedding stress-sensitive active material particles in an aircraft component, the formation of cracks could be detected by identifying changes in the material response of particles in their vicinity. This method, unlike ultrasonic and eddy current NDE, has the advantage of being inherent to the material, eliminating the need for external sensors.

This method revolves around the behavior of shape memory alloys (SMAs). SMAs are a class of materials that can undergo both temperature- and stress-induced solid-to-solid phase transformation, causing a nonlinear change in material response. As an example, consider an SMA particle in the low stress *austenite* phase. As a crack in the vicinity of the particle begins to propagate, the local stress field at the crack tip will increase in magnitude and evolve in spatial distribution; at a certain stress (dictated by particle material properties), the particle will transform into the high-stress *martensite* phase. This phase exhibits altered physical properties and/or mechanical response that can be identified in a variety of manners depending on the material used. This phenomenon is visualized in Figure 1.1. Potential detection method (1) involves the acoustic sensing of phase transformation in SMAs such as NiTi. Oishi and Nagai have demonstrated that acoustic signals from SMA wires could be used to detect changes in strain of up to 5% [52]. Potential detection method (2) uses changes in the electrical resistance of SMAs to detect phase transformation. This

method has been demonstrated by Chatwaranon et al. and Nagai and Oishi [13, 48]. Potential detection method (3) involves the magnetic sensing of martensite generation or variant reorientation in magnetic SMA (MSMA) particles under sufficient stress [32].

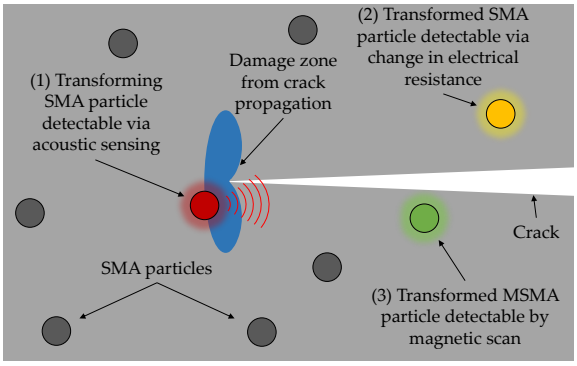

Figure 1.1: Diagram of a NDE method for monitoring fatigue damage using active materials (acoustic, electrical resistance, and magnetic detection options).

Previous work on this detection method has focused on proof-of-concept experiments. In work performed by Leser et al., a fatigue crack was introduced into aluminum 7050 single-edge notch (SEN) specimens containing a layer of NiTi sensory particles [40]. Measurements showed that, as the crack propagated through the specimen, acoustic emissions from regions including the NiTi particles had an amplitude 5-10 times greater than emissions from regions without such sensory particles. Additionally, digital image correlation (DIC) has been used to confirm phase transformation in sensory particles near the growing fatigue crack [40, 15]. These results have motivated computational studies to determine optimal particle dispersion density, size, and shape. However, these studies rely upon the determination of sensory particle material properties, which due to processing techniques can be altered from

those of the bulk material from which they are fabricated. This requires the material properties to be determined based on in-situ measurements.

1.4 Thesis Summary

This thesis serves to describe the first ever computational analysis of the behavior of SMA sensory particles as described and is organized as follows:

- Chapter 2 provides an overview of the experimental and computational tools used in this work. This includes a discussion on the use of digital image correlation to gather experimental data, a derivation of the major material models considered, and a description of several modeling techniques utilized.

- Chapter 3 discusses the finite element modeling of SMA sensory particle response to local structural damage. This model, based on an experimental demonstration of this damage detection method, allows for the determination of sensory particle material properties by matching experimental data to finite element simulations. Material property trends for developing the optimal sensory particle are also discussed.

- Chapter 4 continues to analyze the behavior of sensory particles by computationally demonstrating an application of this damage detection method. Sensory particles are embedded in the vicinity of a propagating crack (modeled using XFEM) in the root rib of an aircraft wing. In particular, this computational model utlizes *substructure modeling* to increase computational efficiency. It is also demonstrated that this damage detection method can approximate the location of structural damage by combining the responses of multiple particles. This is done by using radial basis function (RBF) interpolation to approximate a stress field based on the response of a random configuration of particles.

- Chapter 5 summarizes the results of this work and discusses potential research areas that could expand upon it.

2. OVERVIEW OF EXPERIMENTAL AND COMPUTATIONAL ENGINEERING TOOLS

2.1 Experimental Methods

2.1.1 Full-Field Data Collection

As described in Chapter 1, particle-based sensing of the fatigue crack front requires the initiation of a stress-induced phase transformation in the particles. To identify the potential initiation of this transformation, the mechanical response of a particle must be measured and well understood. This has been made possible using a methodology that combines DIC with scanning electron microscopy (SEM). Referred to hereafter as SEM-DIC, this approach allows for the examination of full-field surface deformations at a microscopic scale. While SEM-DIC enables the relation of macroscopic and microscopic surface deformation, it is hindered by image distortions that are intrinsic to SEM imaging. These distortions can be classified as time-dependent drift distortions and position-dependent spatial distortions [68]. If left uncorrected, these distortions can cause large errors in calculated displacement fields. Kammers and Daly have extensively investigated SEM-DIC, including distortion correction and patterning methods [31, 30]. SEM-DIC has also become an attractive method for analyzing strains related to small-scale phase transformations in SMAs. Work done by Dutta et al. used SEM-DIC to investigate the benefits of using NiTi particles to mitigate strain concentrations in microelectronic solder joints [18]. Kimiecik et al. utilized SEM-DIC to examine phase transformation in NiTi using microscopic strain distributions [35].

SEM-DIC uses randomized and highly-contrasted discontinuities (a "speckle pattern") applied to a material free surface to track local surface displacements, thus

allowing the measurement of the deformation field and associated strain field. If the material being tested does not have a naturally occurring speckle pattern, one can be generated using a number of techniques. Because of the microscopic size of the particles being tested herein, e-beam lithography was applied to the surface area of the particle and surrounding aluminum matrix; this method creates high quality micro-scale speckle patterns [30, 41].

2.2 Mathematical Material Models

2.2.1 Elasto-Plastic Material Model

To accurately simulate the forces acting on a sensory particle, the mechanical response of the surrounding material matrix must be properly modeled. A Mises-type small strain elasto-plastic constitutive model is assumed, such that

$$\boldsymbol{\varepsilon} = \boldsymbol{S}^{AL}\boldsymbol{\sigma} + \boldsymbol{\varepsilon}^{p}, \tag{2.2.1}$$

where $\boldsymbol{\varepsilon}$ is the infinitesimal strain tensor, $\boldsymbol{S}^{AL}$ is the fourth-order compliance tensor for aluminum, $\boldsymbol{\sigma}$ is the stress tensor, and $\boldsymbol{\varepsilon}^{p}$ is the plastic strain tensor. A Mises yield criterion with isotropic hardening is considered [71][25] such that the plastic yield function $\Phi^{p}(\boldsymbol{\sigma}, \bar{\varepsilon}^{p})$ is given by

$$\Phi^{p}(\boldsymbol{\sigma}, \bar{\varepsilon}^{p}) = \bar{\sigma} - f^{p}(\bar{\varepsilon}^{p}), \tag{2.2.2}$$

where $\bar{\sigma}$ is the Mises equivalent stress, $\bar{\varepsilon}^{p}$ is the Mises equivalent plastic strain, and $f^{p}(\bar{\varepsilon}^{p})$ is the isotropic hardening function represented by a table look-up associated with the red curve of Figure 3.7b. The Mises stress is calculated via

$$\bar{\sigma} = \sqrt{\frac{3}{2}\sigma' : \sigma'}, \tag{2.2.3}$$

where σ' is the deviatoric stress. Classical plasticity consistency conditions [36] are given by

$$\Phi^p \leq 0, \qquad \dot{\bar{\varepsilon}}^p \Phi^p = 0, \qquad \dot{\bar{\varepsilon}}^p \geq 0, \tag{2.2.4}$$

where $\dot{\bar{\varepsilon}}^p$ is the Mises equivalent plastic strain rate. The evolution of plastic strain is governed by the relation

$$\dot{\boldsymbol{\varepsilon}}^p = \dot{\bar{\varepsilon}}^p \frac{\partial \Phi^p}{\partial \boldsymbol{\sigma}} = \dot{\bar{\varepsilon}}^p \frac{\partial \Phi^p}{\partial \bar{\sigma}} \frac{\partial \bar{\sigma}}{\partial \boldsymbol{\sigma}} = \dot{\bar{\varepsilon}}^p \frac{3}{2} \frac{\sigma'}{\bar{\sigma}} = \dot{\bar{\varepsilon}}^p \boldsymbol{\Lambda}. \tag{2.2.5}$$

2.2.2 SMA Constitutive Model

A detailed description of the thermomechanical constitutive model for SMAs used is this study can be found elsewhere [36]. However, a brief summary of the simplified version employed herein is provided to elucidate the underlying behavior of this material. The utilized model is three-dimensional, phenomenological, and based on classical plasticity models of the type used for the aluminum in Section 2.2.1. It centers on the generation of transformation strains that occur as a result of reversible martensitic phase transformation. In addition to the stress $\boldsymbol{\sigma}$ and total strain $\boldsymbol{\varepsilon}$ (cf. Section 2.2.1), the model also considers the absolute temperature, T. Two internal state variables are also considered: the inelastic (but generally recoverable) transformation strain $\boldsymbol{\varepsilon}^t$ and the total martensitic volume fraction ξ. Assuming isothermal conditions, the total strain is assumed to be additively decomposed into elastic and transformation terms, and is related to the stress via Hooke's Law (cf. Equation 2.2.1)

$$\boldsymbol{\varepsilon} = \boldsymbol{S}^{SMA}(\xi)\boldsymbol{\sigma} + \boldsymbol{\varepsilon}^t, \tag{2.2.6}$$

where $\boldsymbol{S}^{SMA}(\xi)$ is in general a phase-dependent fourth-order compliance tensor. Here we assume the elastic properties of austenite and martensite are equal, a widely used

assumption in many SMA constitutive models [3, 56, 53], and so $\boldsymbol{S}^{SMA}(\xi)=\boldsymbol{S}^{SMA}$, a tensor of constants.

Phase transformation is initiated and maintained based on a transformation function analogous to the yield function in Equation 2.2.2. Because the experiments and modeled responses considered throughout this work consist of only tensile loading and no unloading is considered, only forward transformation is relevant to the current discussion and only the corresponding branch of Φ^t is considered:

$$\Phi^t_{fwd}(\boldsymbol{\sigma}, T, \xi) = H\bar{\sigma} + p(T, \xi) - Y, \tag{2.2.7}$$

where H is the maximum possible uniaxial transformation strain and $p(T, \xi)$ is a thermodynamic force describing both hardening and the isotropic dependence of transformation stresses on temperature. Constraints inspired by the methods of classical plasticity (cf. Equation 2.2.4) are placed on forward evolution of the martensitic volume fraction ξ and are given by

$$\Phi^t_{fwd} \leq 0, \qquad \dot{\xi}\Phi^t_{fwd} = 0, \qquad \dot{\xi} \geq 0. \tag{2.2.8}$$

An additional constraint is placed on the martensitic volume fraction such that

$$0 \leq \xi \leq 1, \tag{2.2.9}$$

bounding it between 0 (pure austenite) and 1 (pure martensite).

The thermodynamic driving force takes the form [36]

$$p(T, \xi) = \rho\Delta s_0 T - \rho\Delta u_0 - f^t_{fwd}(\xi), \tag{2.2.10}$$

where $\rho\Delta s_0$ represents the entropy difference between austenite and martensite, $\rho\Delta u_0$ represents the internal energy difference between austenite and martensite, and f^t_{fwd} is the transformation isotropic hardening function given by:

$$f^t_{fwd}(\xi) = \frac{1}{2}a_1(1 + \xi^{n_1} - (1-\xi))^{n_2} + a_3. \tag{2.2.11}$$

The smoothness of the transformation hardening function can be tuned by adjusting the members of the set $\{n_1,\ n_2,\ n_3,\ n_4\}$ such that $0 < n_i \leq 1,\ i$=1,...,4. Similar to classical plasticity (cf. Equation 2.2.5), the inelastic transformation strain during loading evolves such that the time rate of change of its magnitude is proportional to the rate of change of the martensitic volume fraction while its direction is normal to Φ^t_{fwd} in the six-dimensional stress space:

$$\dot{\boldsymbol{\varepsilon}}^t \mid_{\dot{\xi}>0} = \dot{\xi}\frac{\partial \Phi^t_{fwd}(\boldsymbol{\sigma})}{\partial \boldsymbol{\sigma}} = \dot{\xi}\Lambda^t_{fwd} = \dot{\xi}H\boldsymbol{\Lambda}. \tag{2.2.12}$$

The transformation parameters $\rho\Delta s_0$, $\rho\Delta u_0$, Y, a_1, and a_3 are defined in Appendix B using SMA phase diagram parameters dicussed in later sections.

A user material subroutine (UMAT in Abaqus) is used to simulate the NiTi particle response. The UMAT employed is a coded numerical implementation of the constitutive model described above [36, 37]. For this study, the particle is assumed to be isotropic. It is also assumed to have undergone no transformation prior to loading (i.e. by nature of the constitutive model described, it begins in the *austenite* phase). Properties associated with reverse transformation (unloading) are not relevant to the current study and are given arbitrary but reasonable constant properties.

2.2.3 Continuum Damage Model

To rigorously simulate damage and potential crack propagation in the specimen during loading, a ductile damage model is introduced to allow predictions of crack propagation in the aluminum matrix. This model [71] extends Equation 2.2.1 to also consider the local degradation of the material. Thus, we introduce an effective (i.e. undamaged) stress tensor is given by

$$\hat{\boldsymbol{\sigma}} = \frac{1}{1-D}\boldsymbol{\sigma}, \tag{2.2.13}$$

where D is a scalar damage variable. Equation 2.2.1 then becomes

$$\boldsymbol{\varepsilon} = \boldsymbol{S}\hat{\boldsymbol{\sigma}} + \boldsymbol{\varepsilon}^p, \tag{2.2.14}$$

and Equation 2.2.2 becomes

$$\Phi^p(\hat{\boldsymbol{\sigma}}, \bar{\varepsilon}^p) = \bar{\hat{\sigma}} - f^p(\bar{\varepsilon}^p). \tag{2.2.15}$$

The extension of the model to consider the effects of damage on elastic response requires two additional considerations: a damage initiation criterion and a damage evolution law [71]. The damage initiation criterion assumes that the equivalent plastic strain at the onset of damage, $\bar{\varepsilon}^p_D$, is given by

$$\bar{\varepsilon}^p_D(\eta, \dot{\bar{\varepsilon}}^p), \tag{2.2.16}$$

where η is the stress triaxiality defined as

$$\eta = \frac{\frac{1}{3}\mathrm{tr}\boldsymbol{\sigma}}{\bar{\sigma}}. \tag{2.2.17}$$

The function $\bar{\varepsilon}^p_D$ is represented here as a table-lookup as given in Appendix C. The criterion for damage initiation is then written in terms of $\bar{\varepsilon}^p_D$ as follows:

$$\omega_D = \int \frac{1}{\bar{\varepsilon}^p_D(\eta, \dot{\bar{\varepsilon}}^p)} d\bar{\varepsilon}^p_D = 1, \tag{2.2.18}$$

where ω_D is the state variable that describes damage initiation. Finally, the damage evolution law governs the rate of degradation of the material stiffness once the damage initiation criterion $\omega_D = 1$ is reached. The damage evolves based on the following equation:

$$\dot{D} = \frac{L\dot{\bar{\varepsilon}}^p}{\sigma_y} 2G_f, \tag{2.2.19}$$

where σ_y is the yield stress at the time when the failure criterion is reached (i.e. $\sigma_y = f^p(\bar{\varepsilon}^p)|_{\omega_D=1}$, cf. Equation 2.2.2), G_f is the fracture energy per unit area, and L is the characteristic length of an element (internally calculated by Abaqus). When $D \to 1$, the material loses its load-bearing capacity; any elements in such state are removed from the analysis, thus providing the representation of a propagating crack desired herein.

This model assumes a proportional loading case, which is not representative of the problem at hand. There are several models that do consider non-proportional loading cases. However, here this damage model is deemed sufficient due to its ease of implementation in Abaqus and its role as simply validating the findings of Section 3.3.2.

2.3 Computational Tools

2.3.1 Substructure Modeling

Substructure modeling is a computationally efficient method of analyzing complex finite element models such as an aircraft wing. The following sections provide

a discussion on the formulation of a substructure, the advantages of using substructure modeling, and a brief example to facilitate understanding of how substructure modeling can be used to reduce computation time.

2.3.1.1 Formulation

A substructure is a collection of elements from which the internal degrees of freedom (DOFs) have been eliminated; only nodes/DOFs specified during the generation of the substructure are retained and recognized externally at the usage level. The reduced stiffness matrix related to all retained nodes is precomputed and retained for later coupling to other domains, including other substructures [71]. Here, we denote the retained DOFs in the substructure, generally located at the boundary, as the vector $\mathbf{u}_b$, while the internal DOFs are denoted as the vector $\mathbf{u}_i$. The objective is to eliminate all internal DOFs through a process called *condensation*. To carry out this condensation process, consider the assembled stiffness equations of a substructure

$$\begin{bmatrix} \mathbf{K}_{bb} & \mathbf{K}_{bi} \\ \mathbf{K}_{ib} & \mathbf{K}_{ii} \end{bmatrix} \begin{bmatrix} \mathbf{u}_b \\ \mathbf{u}_i \end{bmatrix} = \begin{bmatrix} \mathbf{f}_b \\ \mathbf{f}_i \end{bmatrix}. \tag{2.3.20}$$

Taking the second matrix equation

$$\mathbf{K}_{ib}\mathbf{u}_b + \mathbf{K}_{ii}\mathbf{u}_i = \mathbf{f}_i, \tag{2.3.21}$$

and assuming $\mathbf{K}_{ii}$ is nonsingular (i.e. it has a matrix inverse), we can solve for the internal DOFs

$$\mathbf{u}_i = \mathbf{K}_{ii}^{-1}(\mathbf{f}_i - \mathbf{K}_{ib}\mathbf{u}_b). \tag{2.3.22}$$

Substituting Equation 2.3.22 into Equation 2.3.20 yields the condensed stiffness equation

$$\bar{\mathbf{K}}_{bb}\mathbf{u}_b = \bar{\mathbf{f}}_b, \tag{2.3.23}$$

where

$$\bar{\mathbf{K}}_{bb} = \mathbf{K}_{bb} - \mathbf{K}_{bi}\mathbf{K}_{ii}^{-1}\mathbf{K}_{ib}, \tag{2.3.24}$$

and

$$\bar{\mathbf{f}}_b = \mathbf{f}_b - \mathbf{K}_{bi}\mathbf{K}_{ii}^{-1}\mathbf{f}_i. \tag{2.3.25}$$

From here, the condensed substructure may be viewed as a standalone structure whose stiffness matrix and nodal force vector are $\bar{\mathbf{K}}_{bb}$ and $\bar{\mathbf{f}}_b$, respectively.

As a simple example, consider the elements in Figure 2.1, where the interior shared node is designated as DOFs that will be eliminated.
Let us assume that we have the following stiffness equations

$$\begin{bmatrix} 7 & -9 & -3 & 4 & 10 & -9 & -8 & -2 & 9 \\ 2 & -9 & -7 & 5 & -9 & -2 & 8 & -9 & 0 \\ 1 & 1 & 6 & -1 & -1 & -5 & 2 & -5 & 0 \\ 9 & 6 & -4 & -9 & -8 & 6 & 1 & -8 & -3 \\ -4 & 9 & 1 & -6 & 10 & -1 & -7 & -7 & 8 \\ 5 & -8 & -7 & 9 & -10 & 9 & 7 & -5 & -3 \\ 5 & 1 & 2 & -7 & 6 & -7 & 3 & -2 & -8 \\ -3 & -1 & -5 & 7 & 7 & -5 & -3 & -9 & 6 \\ 1 & -10 & 3 & 1 & 8 & -7 & 0 & 8 & -2 \end{bmatrix} \begin{bmatrix} u_1 \\ u_2 \\ u_3 \\ u_4 \\ u_5 \\ u_6 \\ u_7 \\ u_8 \\ u_9 \end{bmatrix} = \begin{bmatrix} -5 \\ -2 \\ -8 \\ -8 \\ 9 \\ 10 \\ 2 \\ -9 \\ -6 \end{bmatrix}. \tag{2.3.26}$$

Suppose that the last displacement freedom vector, $\mathbf{u}_9$, is the vector associated with the interior node that must be condensed out. Equation 2.3.26 can then be written

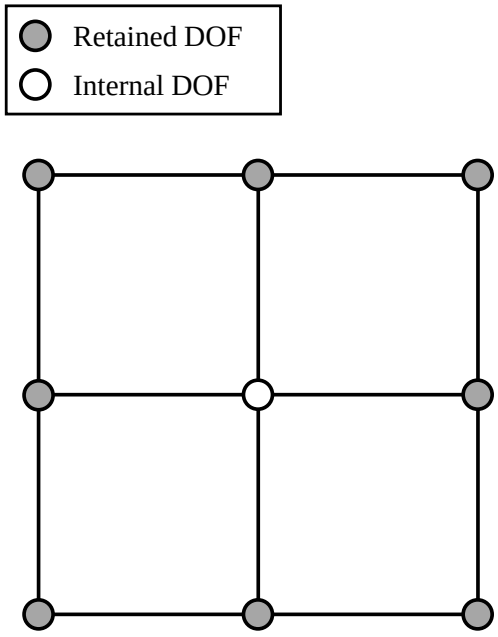

Figure 2.1: Example elements for the demonstration of calculating the condensed substructure stiffness matrix.

in terms of Equation 2.3.20 using the following relations:

$$\mathbf{K}_{bb} = \begin{bmatrix} 7 & -9 & -3 & 4 & 10 & -9 & -8 & -2 \\ 2 & -9 & -7 & 5 & -9 & -2 & 8 & -9 \\ 1 & 1 & 6 & -1 & -1 & -5 & 2 & -5 \\ 9 & 6 & -4 & -9 & -8 & 6 & 1 & -8 \\ -4 & 9 & 1 & -6 & 10 & -1 & -7 & -7 \\ 5 & -8 & -7 & 9 & -10 & 9 & 7 & -5 \\ 5 & 1 & 2 & -7 & 6 & -7 & 3 & -2 \\ -3 & -1 & -5 & 7 & 7 & -5 & -3 & -9, \end{bmatrix} \tag{2.3.27}$$

$$\mathbf{K}_{bi} = \begin{bmatrix} 9 & 0 & 0 & -3 & 9 & -3 & -8 & 6 \end{bmatrix}^T, \tag{2.3.28}$$

$$\mathbf{K}_{ib} = \begin{bmatrix} 1 & -10 & 3 & 1 & 8 & -7 & 0 & 8 \end{bmatrix}, \tag{2.3.29}$$

$$\mathbf{K}_{ii} = \begin{bmatrix} -2 \end{bmatrix}, \tag{2.3.30}$$

$$\mathbf{u}_b = \begin{bmatrix} u_1 & u_2 & u_3 & u_4 & u_5 & u_6 & u_7 & u_8 \end{bmatrix}^T, \tag{2.3.31}$$

$$\mathbf{u}_i = \begin{bmatrix} u_9 \end{bmatrix}, \tag{2.3.32}$$

$$\mathbf{f}_b = \begin{bmatrix} -5 & -2 & -8 & -8 & 9 & 10 & 2 & -9 \end{bmatrix}^T, \tag{2.3.33}$$

$$\mathbf{f}_i = \begin{bmatrix} -6 \end{bmatrix}. \tag{2.3.34}$$

Equations 2.3.27-2.3.34 can be substituted into Equations 2.3.24-2.3.25 to obtain

$$\bar{\mathbf{K}}_{bb} = \begin{bmatrix} \frac{23}{2} & -54 & \frac{21}{2} & \frac{17}{2} & 46 & \frac{-81}{2} & -8 & 34 \\ 2 & -9 & -7 & 5 & -9 & -2 & 8 & -9 \\ 1 & 1 & 6 & -1 & -1 & -5 & 2 & -5 \\ \frac{15}{2} & 21 & \frac{-17}{2} & \frac{-21}{2} & -20 & \frac{33}{2} & 1 & -20 \\ 0 & -31 & 13 & -2 & 42 & -19 & 7 & 27 \\ \frac{7}{2} & 7 & \frac{-23}{2} & \frac{15}{2} & -22 & \frac{39}{2} & 7 & -17 \\ 1 & 41 & -10 & -11 & -26 & 21 & 3 & -34 \\ 0 & -31 & 4 & 10 & 31 & -26 & -3 & 15 \end{bmatrix}, \tag{2.3.35}$$

$$\bar{\mathbf{f}}_b = \begin{bmatrix} -32 & -2 & -8 & 1 & -15 & 19 & 26 & -27 \end{bmatrix}^T. \tag{2.3.36}$$

2.3.1.2 Computational Advantages and Limitations

Substructure modeling has various computational advantages, such as

1. Due to the retention of only specified nodes, the stiffness matrix associated with a part's substructure is relatively small compared to the part's initial stiffness matrix.

2. The stiffness matrix of a substructure is calculated only once and then stored, improving efficiency when analyzing an unchanged part in multiple models or when the same part is used in a model multiple times.

3. Substructure modeling allows for large and complex models to be built as nested substructures, built up level by level until the whole structure is complete.

There are, however, several limitations to using substructures. First, there is a limitation to the number of DOFs that can be retained in each analysis. Second, the response of the substructure domain must be linear. This prevents the use of

substructure modeling on parts containing SMA material. (There are substructure models that allow for nonlinear responses, such as one developed by Wu and Haug [77], but these are beyond the scope of this study). Nevertheless, substructure modeling has become a viable method for modeling complex structures. Dougherty et al. have implemented substructure modeling to examine plasticity-induced crack closure in steel [17]. Additionally, substructure modeling has also been utilized to model fatigue crack growth in marine structures [66, 24].

2.3.1.3 Substructure Example

To facilitate an understanding of how substructure modeling is used, consider the simple academic example in Figure 2.2. Suppose we wish to perform a study on how changes in the fillet size affect the response of this bar while every other aspect remains constant. Figure 2.3a shows the stress distribution in the small box; this calculation took 28 s. Each time the fillet size is changed the entire problem is recalculated, including the domains that are not changing.

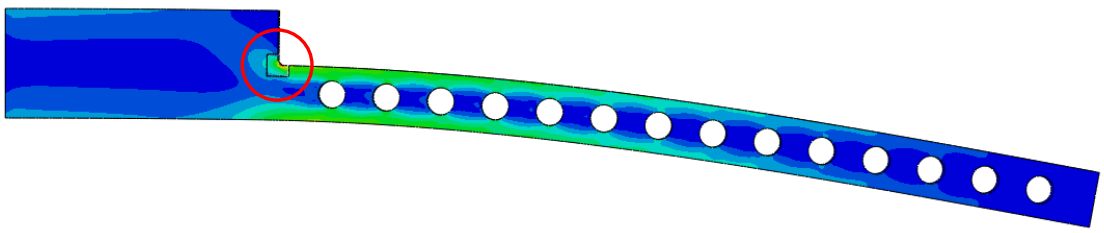

Figure 2.2: Academic problem demonstrating the use of substructure modeling. The region of interest is the small box denoted by the red circle.

Now suppose we designate the domains of the bar that are not changing (i.e. the entire bar minus the small box) as a substructure. The stiffness matrix of the larger

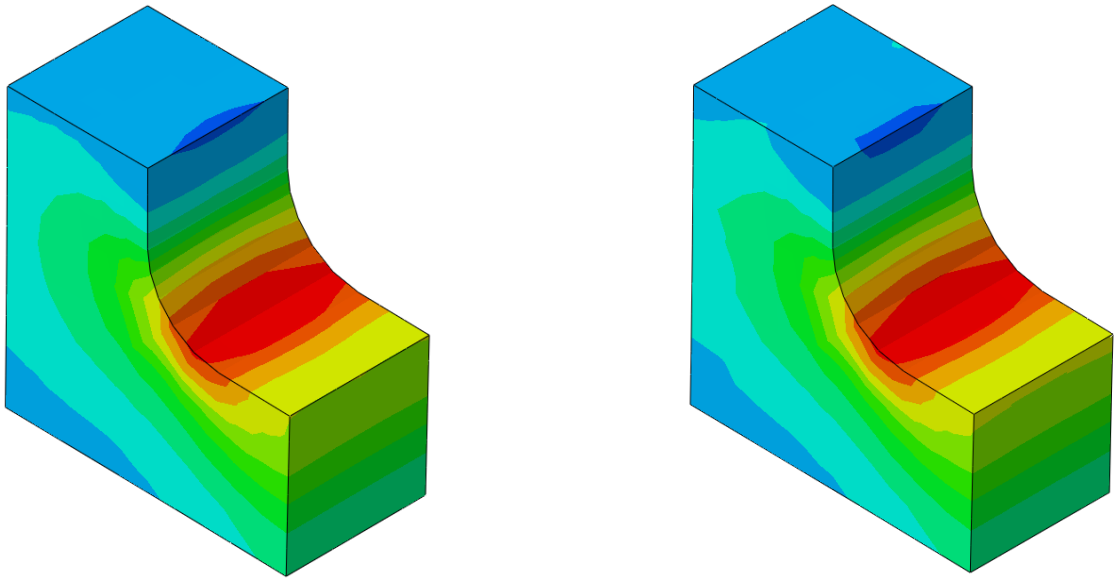

(a) Response when considering the entire bar as a solid part.

(b) Response when designating the beam as a substructure.

Figure 2.3: Comparison of bar response using both modeling methods. Note that while the responses are approximately the same, substructure modeling reduces the computation time by nearly two-thirds.

bar is calculated during substructure generation and is then stored. Each time the fillet size is changed and analysis begins, the stiffness matrix of the bar is recalled and coupled to the domain of interest. Figure 2.3b shows the stress distribution in the small box with the beam designated as a substructure; this analysis took 11 s. Note that while the response of the small box is approximately the same, the use of substructure modeling reduced computation time by nearly two-thirds.

2.3.2 Extended Finite Element Method

Modeling cracks with the conventional finite element method requires the mesh to conform to the geometric discontinuities that arise. Considerable mesh refinement is necessary around the crack tip to capture near-tip asymptotic singularity

behavior. Modeling crack propagation causes further complications, as the mesh must be continuously updated to conform to the discontinuities that are moving as the crack tip advances. The extended finite element method (XFEM), developed by Belytschko and Black [6], alleviates these complications by allowing local enrichment functions to be incorporated into a finite element approximation. These enrichment functions allow the presence of discontinuities while retaining a finite element framework and its properties. The result is the propagation of a crack along an arbitrary, solution-dependent path in a bulk material [71].

The enrichment function typically consists of near-tip asymptotic functions that provide the singularity behavior around the crack tip, as well as a discontinuous function that represents the jump in displacement across crack surfaces [55]. In this work, it is assumed that crack propagation is not tied to the element boundaries in a mesh, making the inclusion of near-tip asymptotic functions unnecessary. This assumption forces the crack to propagate across an entire element at a time. The approximation for a displacement vector $\mathbf{u}$ in an enriched domain is then given by

$$\mathbf{u} = \sum_{i=1}^{n} N_i(x) \left[\mathbf{u}_i + H(x)\mathbf{a}_i \right], \tag{2.3.37}$$

where $N_i(x)$ are the typical nodal shape functions, $\mathbf{u}_i$ is the nodal displacement vector associated with the continuous part of the finite element solution, $H(x)$ is the Heaviside function associated with the discontinuous jump across the crack surfaces, and $\mathbf{a}_i$ is the nodal enriched degree of freedom vector. The Heaviside function is given as

$$H(x) = \begin{cases} 1, & \text{if } (\mathbf{x} - \mathbf{x}^*) \cdot \mathbf{n} \geq 0 \\ -1, & \text{if } (\mathbf{x} - \mathbf{x}^*) \cdot \mathbf{n} \leq 0, \end{cases} \tag{2.3.38}$$

where $\mathbf{x}$ is a sample point, $\mathbf{x}^*$ is the point on the crack closest to $\mathbf{x}$, and $\mathbf{n}$ is the unit

outward normal to the crack at $\mathbf{x}^*$ (Figure 2.4).

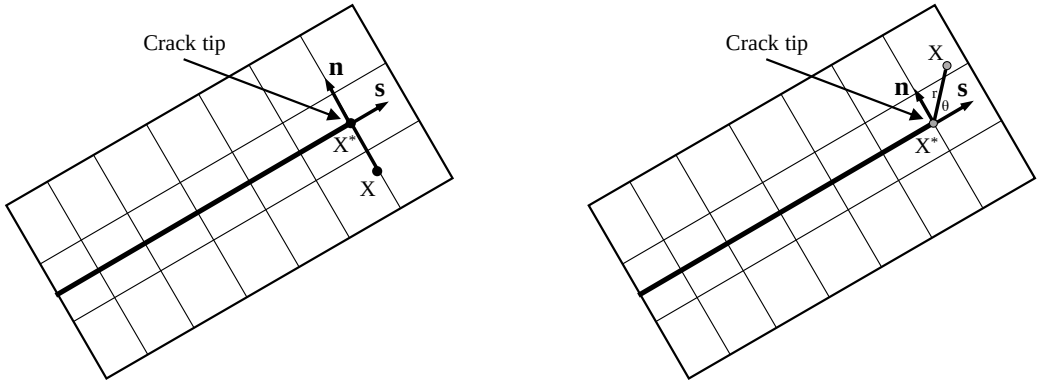

(a) Normal Coordinates. (b) Tangential Coordinates.

Figure 2.4: Illustration of the discontinuous jump function across the crack surface.

The movement of the crack is based on the principles of linear elastic fracture mechanics (LEFM), as well as the utilization of *phantom nodes* [71]. When an element is intact, each phantom node is constrained to its corresponding real node. The phantom node is allowed to separate from its real node when the equivalent strain energy release rate exceeds the critical strain energy specified by the user (i.e. when the element splits into two parts). Thus, an element is represented by a combination of real and phantom nodes (Figure 2.5). This method has proven to exhibit minimal mesh dependency if the initial mesh is sufficiently refined.

2.4 Other Numerical Tools

2.4.1 Optimization Framework

After the sensory particle method is demonstrated using finite element analysis, an optimization framework will be used to match experimental strain data to

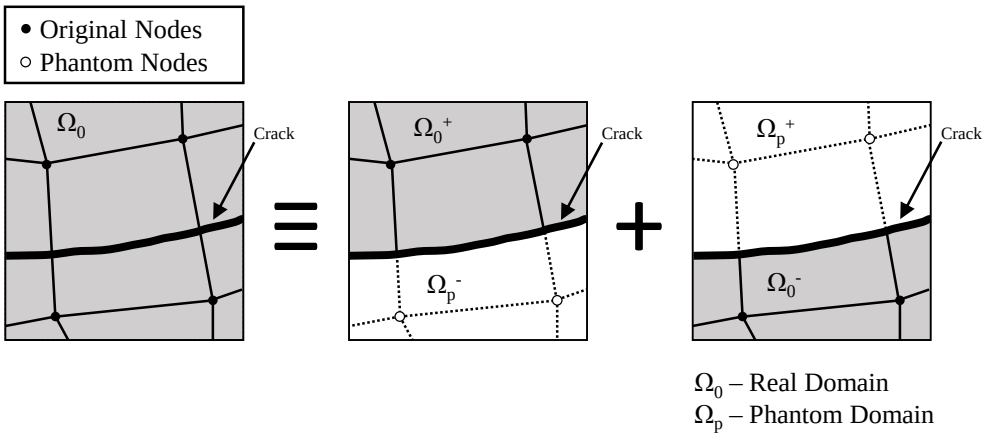

Figure 2.5: Depiction of the phantom node method.

simulated results. This section will provide a brief discussion on the optimization algorithm utilized.

Most numerical optimization methods are iterative algorithms that consider a sequence of guesses, $\mathbf{x}_n$, which will ultimately converge to $\mathbf{x}^*$, the true global minimizer of some function f. This process can be done using Newton's Method, which is used to find successively better approximations to the roots of a real-valued function [43]. At a minimum of some function f, it can be shown that $\nabla f(\mathbf{x}^*) = 0$. Thus, Newton's Method can be used to approximate the value of x which satisfies $\nabla f(\mathbf{x}^*) = 0$, assuming that $f(\mathbf{x})$ is twice-differentiable. Neglecting higher-order terms, the Taylor series expansion of $f(\mathbf{x})$ around the point $\mathbf{x} = \mathbf{x}_n$ is given as

$$f(\mathbf{x}) \approx f(\mathbf{x}_n) + \nabla f^T(\mathbf{x}_n)(\mathbf{x}_{n+1} - \mathbf{x}_n) + \frac{1}{2}(\mathbf{x}_{n+1} - \mathbf{x}_n)^T \mathbf{H}_n (\mathbf{x}_{n+1} - \mathbf{x}_n), \quad (2.4.39)$$

where $\mathbf{H}_n$ is the Hessian matrix at $\mathbf{x} = \mathbf{x}_n$. Herein we will assume that the Hessian is a symmetric positive definite matrix. Taking the derivative of the Taylor expansion,

we obtain

$$\nabla f(\mathbf{x}) \approx \nabla f(\mathbf{x}_n) + \mathbf{H}_n(\mathbf{x}_{n+1} - \mathbf{x}_n). \tag{2.4.40}$$

Recalling that $\nabla f(\mathbf{x}) = 0$ at the minimum of f and rearranging, we are left with

$$\mathbf{x}_{n+1} \approx \mathbf{x}_n - \mathbf{H}_n^{-1}\nabla f(\mathbf{x}_n). \tag{2.4.41}$$

Using this equation, one can iterate until the solution converges to some minimizer $\mathbf{x}^*$. While this method can converge to the minimum in a few iterations, it becomes computationally expensive when considering large numbers of parameters. This is because each iteration of Newton's method requires the calculation of the gradient, Hessian, and inverse of the Hessian; large numbers of parameters makes computing the Hessian or its inverse impractical or even impossible.

Rather than contending with computing the Hessian and its inverse during every iteration, the optimization framework instead relies on a quasi-Newton formula, which approximates $\mathbf{H}_n$ in such a way that it has certain properties of the true Hessian [16]. This is ensured by using the secant equation, given by

$$\mathbf{H}_n(\mathbf{x}_n - \mathbf{x}_{n-1}) = \nabla f(\mathbf{x}_n) - \nabla f(\mathbf{x}_{n-1}). \tag{2.4.42}$$

Setting

$$\mathbf{s}_n = \mathbf{x}_n - \mathbf{x}_{n-1}, \tag{2.4.43}$$

and

$$\mathbf{y}_n = \nabla f(\mathbf{x}_n) - \nabla f(\mathbf{x}_{n-1}), \tag{2.4.44}$$

Equation 2.4.42 becomes

$$\mathbf{H}_n\mathbf{s}_n = \mathbf{y}_n, \tag{2.4.45}$$

or equivalently

$$\mathbf{H}_n^{-1}\mathbf{y}_n = \mathbf{s}_n. \tag{2.4.46}$$

This requirement, along with the assumption that the Hessian is a symmetric positive definite matrix, is not enough to uniquely determine $\mathbf{H}_n$. To do that, we require

$$\mathbf{H}_n = \arg\min \| \mathbf{H}_n - \mathbf{H}_{n-1} \|, \tag{2.4.47}$$

i.e. that $\mathbf{H}_n$ be the closest to $\mathbf{H}_{n-1}$ among all symmetric positive definite matrices that satisfy Equation 2.4.42 [62]. The choice of the matrix norm used leads to various Hessian update formulas, and thus various quasi-Newton algorithms.

The most popular quasi-Newton formula, and the one that is used in this work, is the Broyden-Fletcher-Goldfarb-Shanno (BFGS) optimization algorithm provided in SciPy (Scientific Python) [29], which has shown good performance for constrained non-smooth optimization [51]. The update algorithm is given by

$$\mathbf{H}_n^{-1} = (\mathbf{I} - \boldsymbol{\rho}_n \mathbf{y}_n \mathbf{s}_n^T)\mathbf{H}_{n-1}^{-1}(\mathbf{I} - \boldsymbol{\rho}_n \mathbf{y}_n \mathbf{s}_n^T) + \boldsymbol{\rho}_n \mathbf{s}_n \mathbf{s}_n^T, \tag{2.4.48}$$

where $\mathbf{I}$ is the identity matrix and $\boldsymbol{\rho}_n = (\mathbf{y}_n^T \mathbf{s}_n)^{-1}$. In particular, this work uses the Limited-Memory Bounded BFGS (L-BFGS-B), which stores information from the past m iterations to represent the approximation of the inverse Hessian implicitly [50] and can handle simple box constraints.

2.4.2 Radial Basis Function Interpolation

As mentioned in Chapter 1, a section of this work will demonstrate that SMA sensory particle response can be used to approximate the location of structural damage. This involves approximating a stress field given the response of several particles

using radial basis function (RBF) interpolation. An RBF is a real-valued function whose values depend solely on the Euclidean distance between a given point and some pre-specified point. They can be used to build up a function approximation (i.e. an interpolated stress field) of the form

$$y(\mathbf{x}) = \sum_{i=1}^{n} w_i \phi(\| \mathbf{x} - \mathbf{x}_i \|), \tag{2.4.49}$$

where n is the number of discrete points provided, w is a weighted coefficient calculated using the discrete data, and ϕ is the RBF kernel. While there are several different RBF kernels, for this problem we use the *inverse form* given by

$$\phi(\| \mathbf{x} - \mathbf{x}_i \|) = \frac{1}{\sqrt{1 + (\varepsilon \| \mathbf{x} - \mathbf{x}_i \|)^2}}, \tag{2.4.50}$$

where ε is a shape parameter approximated as the average distance between between the given points [29]. A detailed discussion on the use of the inverse RBF as compared to other kernel forms can be found in Appendix A; here it will suffice to say that the inverse RBF is reliable with both dense and sparse data, and was shown to better capture the expected behavior of the problem.

To illustrate this interpolation method, consider the problem in Figure 2.6. The coordinates and values of these points are entered into an open-source SciPy implementation of RBF interpolation [29]. The weights are solved by a system of linear equations inside the SciPy implementation. Thus, Equation 2.4.49 becomes

$$y(x, y) = \sum_{i=1}^{9} \frac{w_i}{\sqrt{1 + (\varepsilon \sqrt{(x - x_i)^2 + (y - y_i)^2})^2}}, \tag{2.4.51}$$

where

$$\begin{aligned}\mathbf{w} &= [w_1, w_2, w_3, w_4, w_5, w_6, w_7, w_8, w_9] \\ &= [4.99, 12.90, -26.16, 16.36, 4.17, -20.67, -3.20, -4.70, 16.45]\,,\end{aligned} \tag{2.4.52}$$

$$\varepsilon = 0.667, \tag{2.4.53}$$

$$\begin{aligned}\mathbf{x} &= [x_1, x_2, x_3, x_4, x_5, x_6, x_7, x_8, x_9] \\ &= [1.0, 1.0, 1.0, 2.0, 3.0, 3.0, 3.0, 2.0, 2.0]\,,\end{aligned} \tag{2.4.54}$$

and

$$\begin{aligned}\mathbf{y} &= [y_1, y_2, y_3, y_4, y_5, y_6, y_7, y_8, y_9] \\ &= [1.0, 2.0, 3.0, 3.0, 3.0, 2.0, 1.0, 1.0, 2.0]\,.\end{aligned} \tag{2.4.55}$$

The result of Equation 2.4.51 is shown in Figure 2.7.

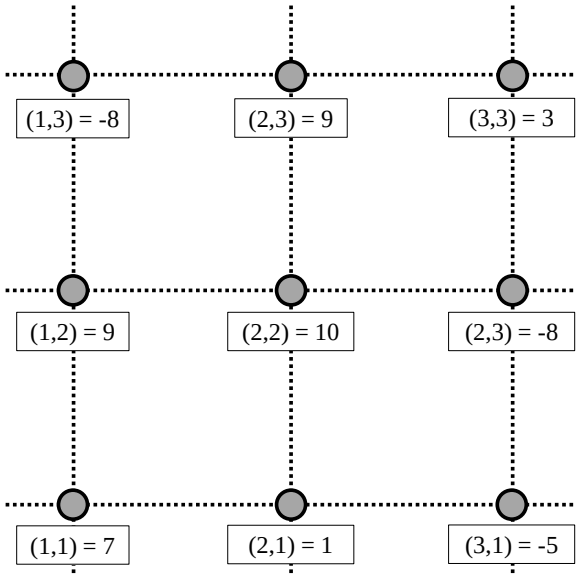

Figure 2.6: Example points for the demonstration of radial basis function interpolation.

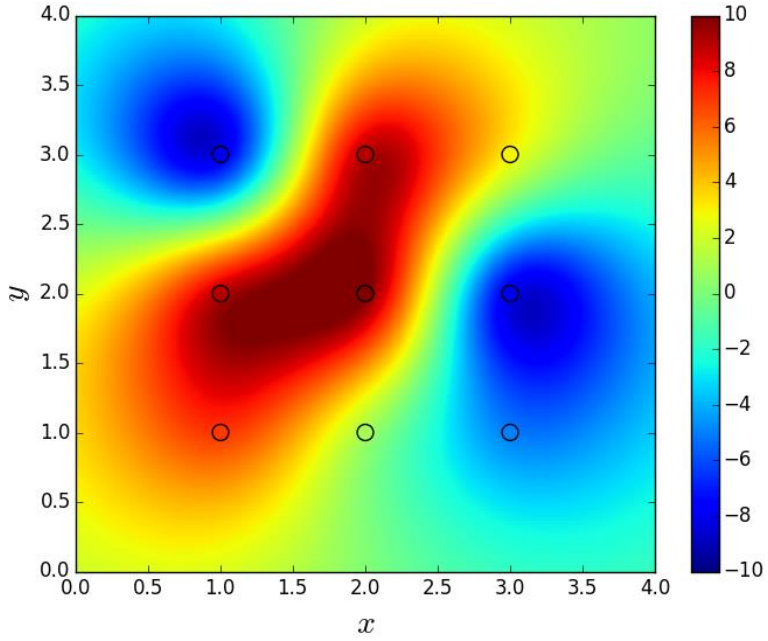

Figure 2.7: Result of example problem given in Figure 2.6 and Equation 2.4.51.

3. EXPERIMENTAL AND COMPUTATIONAL ASSESSMENT OF SMA SENSORY PARTICLE RESPONSE TO LOCAL STRUCTURAL DAMAGE

As was discussed in Chapter 1, the successful implementation of this novel NDE method depends on an accurate understanding of the SMA particle response. This can be achieved by constructing an accurate finite element model of the system and calibrating the response of the SMA particles in particular using experimental full-field strain data gathered using image correlation systems [75]. Similar work by Chemisky et al. demonstrated the ability to approximate the material parameters of a NiTi alloy such that complex predictions of its behavior could be computed with a relative error of less than 1% [14]. Once a constitutive model is calibrated and accurate predictions of embedded particle response are obtained, the optimal placement, size, and shape of sensory particles for the detection of fatigue cracks can be determined.

3.1 Experimental Demonstration of Concept

3.1.1 Specimen Preparation

A single-edge notch (SEN) specimen was fabricated for fatigue testing using aluminum alloy 7050 with embedded spherical NiTi SMA particles. NiTi particles, $\sim$100 μm-diameter, were first distributed onto an aluminum plate and a second identical aluminum plate was placed on top, sandwiching the layer of particles. The plates were then hot-pressed together in a vacuum at 525°C under a pressure of 35 MPa for 1 hr to create a single bulk plate (Figure 3.1). This bulk plate was solutionized at 490°C for 6 hours and peak aged at 121°C for 24 hours in a vacuum before the SEN specimen was cut from the plate using electrical discharge machining (EDM). Figure 3.2 illustrates the tested specimen and provides its dimensions.

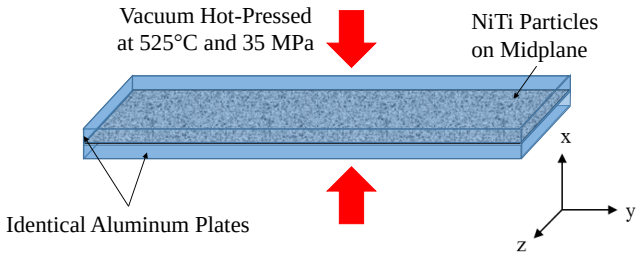

Figure 3.1: Manufacturing of the AL7050/NiTi bulk plate (schematic).

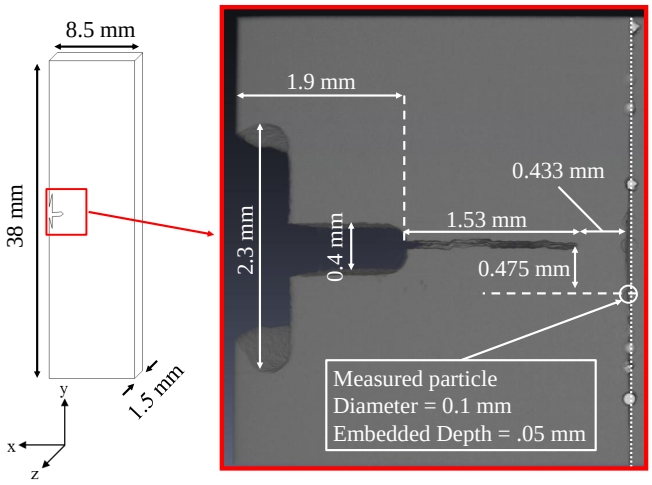

Figure 3.2: Experimental SEN specimen (cf. the orientation in Figure 3.1). The white dotted vertical line on the far right signifies the hot press interface. Image depicts specimen at the end of loading to catastrophic failure (not modeled).

To assess the real-world application of this detection method as described in Chapter 1, a pre-crack was introduced into the SEN specimen prior to monotonic

mode I loading. This was achieved by fatigue cycling using a table-top MTS® with a constant ΔK of 4.40 MPa$\sqrt{m}$, load ratio of R=0.1, at 20 Hz (sinusoidal loading). The fatigue crack was extended to 1.53 mm for a total pre-crack length of 3.43 mm, with the crack tip 0.433 mm from the hot press interface and is shown in Figure 3.3.

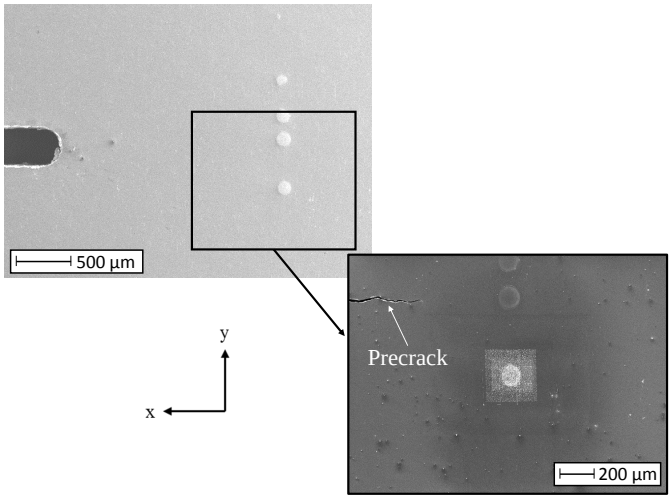

Figure 3.3: View of the pre-crack before loading.

3.1.2 Testing

As a means of characterizing SMA particle response, 2D SEM-DIC (cf. Section 2.1.1) was utilized to generate full-field strain data for the area surrounding a particle 0.475 mm away from the crack and embedded one-half diameter into the matrix (as shown in Figure 3.2). The SEN specimen was subjected to uniaxial-loading (i.e. mode I fracture testing) in a MTII/Fullam® load-frame with a load capacity of 4,400 N. The 2D SEM-DIC measurements were conducted in-situ; images were acquired 30 seconds after each load increment, with pairs of images being col-

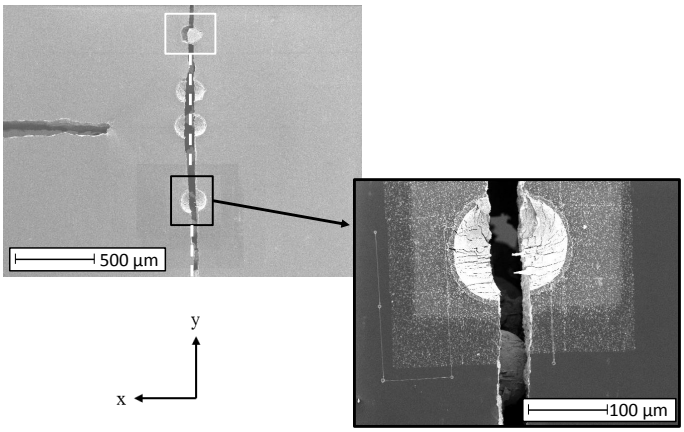

Figure 3.4: Local SEM-DIC pattern (inset) as observed on the SEN specimen after failure. The specimen failed catastrophically along the hot press interface (white dashed line). This final cracking initiated either particle fracture (black box and inset) or decohesion of the particle from the aluminum host material (white box).

lected to account for drift distortions [68]. Strain data was collected pointwise and is also considered herein in terms of the average strain measured on the particle face, given by

$$\hat{\boldsymbol{\varepsilon}}^{exp} = \frac{1}{A}\int \boldsymbol{\varepsilon}^{exp}(x,y)\mathrm{d}A \approx \frac{1}{A}\sum_{i=1}^{m} \boldsymbol{\varepsilon}_i^{exp} a_i, \tag{3.1.1}$$

$$\boldsymbol{\varepsilon}^{exp} = \{\varepsilon_{xx}^{exp}, \varepsilon_{yy}^{exp}, \varepsilon_{xy}^{exp}\}^T, \tag{3.1.2}$$

where A is the exposed surface area of the entire particle, m is the number of data points taken using SEM-DIC, and a_i is the surface area corresponding to the specified data point i.

The specimen was loaded to approximately 1,800 N (400 lb_f), at which point it failed along the NiTi hot press interface (Figure 3.4). It is believed that this failure, orthogonal to the expected Mode I fracture surface, is due to the fatigue crack

tunneling towards and reaching the weaker hot press interface within the specimen, at which point it was redirected along the interface. Failure caused either the fracture of particles along the axis of failure or, as seen in the top particle (white box), decohesion of the particle from one of the aluminum plates[1] Figure 3.5 shows $\hat{\varepsilon}_{yy}^{exp}$ as a function of load along with strain fields generated using 2D SEM-DIC for the particle highlighted in Figure 3.2. Note that experimental data at loads above 1,400 N (designated by the dashed line in Figure 3.5) are not considered herein. This will be discussed in Section 3.2.1.

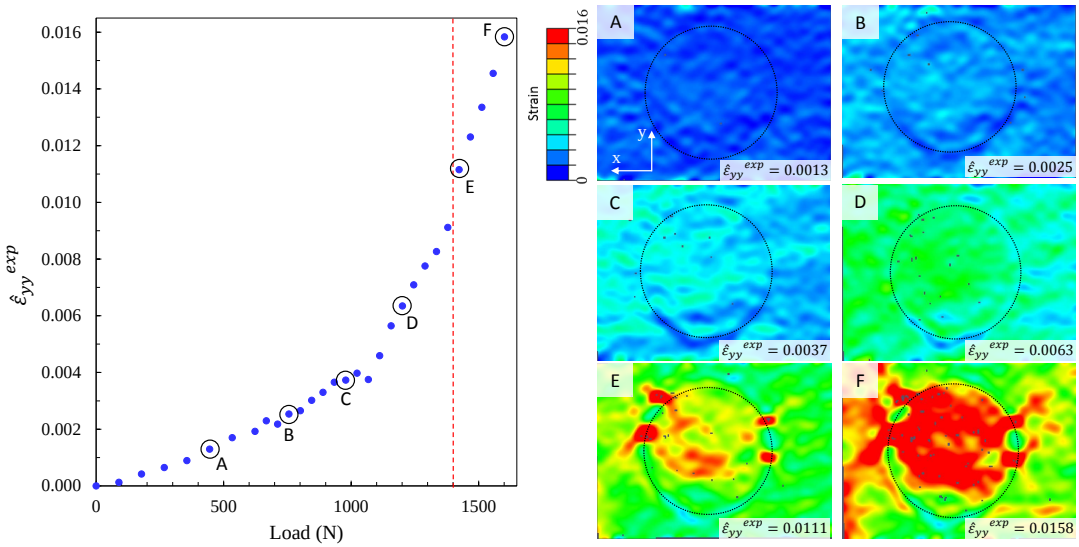

Figure 3.5: Average strain in the mode I loading direction as a function of applied load during the experiment and associated strain fields (A-F) generated at corresponding loads. Data at loads above 1,400 N (dashed line) is not considered.

[1]It is important to note that the manufacturing process described in this experiment is not representative of how the particles would be embedded in components during implementation and is being used for this initial proof of concept only. This issue is currently being researched.

3.2 Computational Model

Understanding the stress-induced response of the embedded NiTi particles requires an engineering model that can predict results similar to those from the experiment of Section 3.1. To this end, a structural model is constructed using the Simulia Abaqus FEA package [71] and the specimen dimensions shown in Figure 3.2. To reduce computation time, only the half of the specimen that includes the particle of interest (denoted by the black box in Figure 3.2) is modeled; symmetry constraints are applied to the negative y-face of the model (excluding the traction-free pre-cracked face).To further increase FEA efficiency, the model is constructed from discrete sections that increase the mesh refinement near the particle crack using surface-based "tie" constraints [71]. This constraint equalizes the translational and rotational motion for a pair of tied surfaces, thus allowing for rapid transitions in mesh density (Figure 3.6b). The model consists of 104,502 second-order hexahedral elements with reduced integration, with greater mesh density in the area surrounding the particle. The appropriate mesh densities were selected by running mesh convergence studies to determine at what mesh size the results of the finite element simulation converge; attempts were made to keepp mesh transition ratios at approximately 2:1. To restrict rigid body translations/rotations, zero-displacement boundary conditions are applied in the x- and z-direction to nodes at a specific point and along a specific line in the y-z plane as shown in Figure 3.6a. A distributed pressure load is applied to the top of the model in the positive y-direction (Figure 3.6a), simulating a far-field tensile stress field. Note that the hot press interface is modeled as being equal in failure strength to the remainder of the matrix; localized cohesive failure in this region is not considered. The model is loaded to approximately 1,800 N using the same load increments as the experiment at a constant temperature of 298 K. There are

29 analysis steps, one for each load increment at which experimental full-field strain data was captured during the experiment.

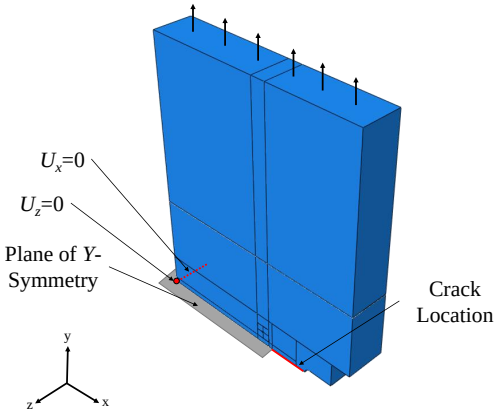

(a) The SEN specimen and boundary conditions.

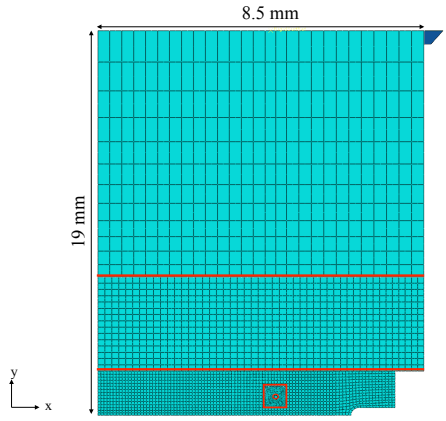

(b) Location of surface-based tie constraints for mesh transitions (shown by bold lines).

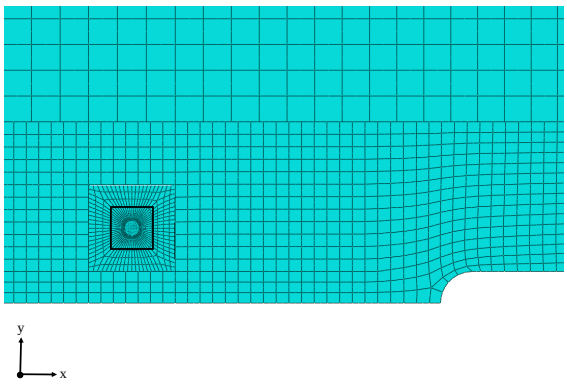

(c) The NiTi particle (shown in the box) embedded in the aluminum specimen.

Figure 3.6: FEA model of the aluminum specimen with embedded sensory particle.

To accurately simulate the forces acting on a sensory particle, the behavior of the aluminum matrix surrounding the particle is calibrated using the model described in Section 2.2.1. An aluminum test specimen of the same composition as the specimen

matrix was uniaxially-loaded to approximately 500 MPa then unloaded to approximately 275 MPa. Using a stress-strain curve from the experiment, the Young's modulus of the aluminum was estimated to be 74 GPa and the plastic hardening was assessed. Comparison of the experimental and analytical aluminum stress-strain curves are shown in Figure 3.7.

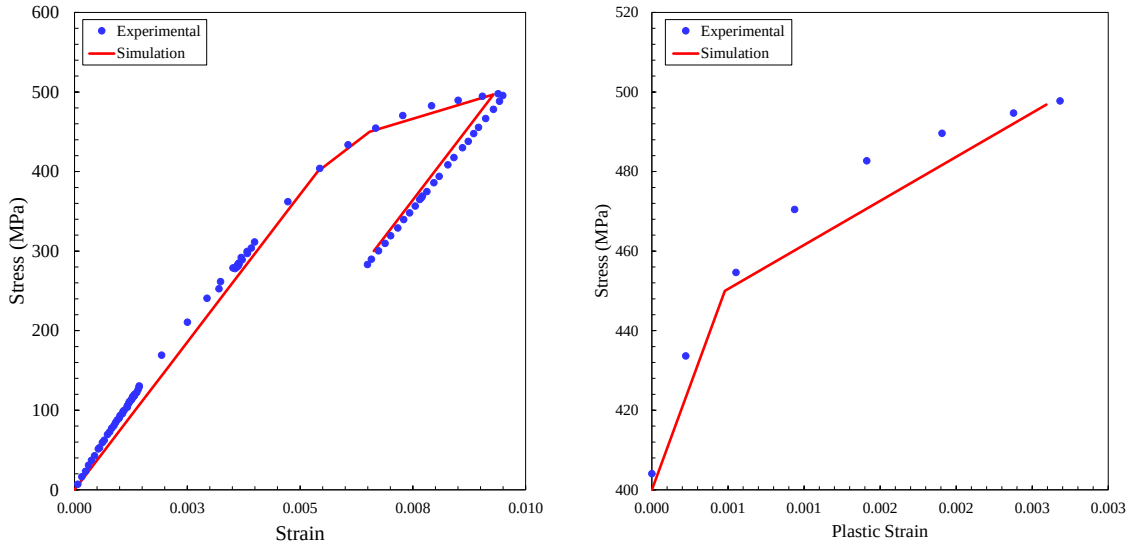

(a) Stress versus total strain.

(b) Stress versus plastic strain.

Figure 3.7: Experimental and simulated stress-strain curves for Al7050 representing calibration of the elasto-plastic model.

The behavior of the SMA sensory particle is governed by the constitutive model discussed in Section 2.2.2. For this preliminary study, the SMA material properties are shown in Table 3.1. As mentioned in Section 2.2.2, the Young's modulus of martensite, E_M, is assumed to be equal to that of austenite, E_A. Thus, we must

consider the calibration of

$$\mathbf{s} = \{E_A, M_s, (M_s - M_f), H\} \tag{3.2.3}$$

where $\mathbf{s}$ is the unknown set of material properties associated with the particle illustrated in Figure 3.3, M_s is the martensitic start temperature, $M_s - M_f$ is the difference between the martensitic start and martensitic finish temperatures, and H is the maximum possible uniaxial transformation strain.

Table 3.1: SMA material properties held constant during the study (i.e. not optimized) due to a lack of experimental data or to reduce the number of parameters.

	Parameter	Value
Elastic Properties	$\nu^A = \nu^M$	0.33
Phase Diagram Properties	A_s	311 K
	A_f	332 K
	C_A=C_M	7.0 MPa/K
Transformation Properties	$n_1 = n_2 = n_3 = n_4$	1.0

3.2.1 Approximation of Crack Propagation During Loading

As seen in Figure 3.5, at a load of approximately 1,100 N the relationship between local particle strain rate and global load steepens noticeably. Based on experimental observations, this is believed to have been caused by damage evolution in the specimen in the form of crack propagation, causing an associated stress concentration to move toward and eventually envelop the particle. However, the propagation of

the crack and evolution of its internal profile were not quantified. Introduction of the damage model to account for crack growth in the matrix will be considered in Section 3.4. However, it was found to be too computationally expensive for use in iterative SMA material property identification.

To approximate the crack evolution for the purposes of SMA particle model calibration, it is assumed that the crack begins propagating at the previously specified load (1,000 N) and reaches the hot press interface at the end of loading (approximately 1,600 N). It is further assumed that the crack propagated at a constant rate during that period (i.e. that the crack front is represented by a straight line segment aligned with the z-axis). The crack is thus propagated across the entire thickness of the specimen using a node-release technique on the negative y-surface of the model [28, 1, 78, 72]. This was found to be a computationally inexpensive approximation and will be validated in Section 3.4. Figure 3.8 shows the movement of the stress concentration past the particle for one example analysis. In this simulation, the strength of the stress field around the particle subsides after approximately 1,300 N. However, in the experiment the strain on the particle face continued to increase. This could be contributed to additional stress concentrations caused by fracturing along the hot press interface orthogonal to the mode I crack, which is not modeled in this work (cf. Figure 3.4). Given this difference in behavior and the lack of interest in analyzing failure at the hot press interface, only the response of the particle up to 1,350 N is considered herein.

3.2.2 Determination of Material Properties

In general, the transformation response of a particle to a nearby crack is clearly dependent upon its material properties, which may have been altered from bulk values during material/specimen processing. These properties are then unknown and

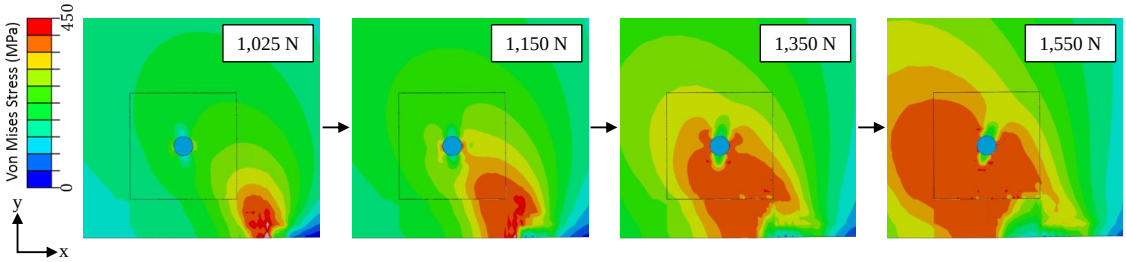

Figure 3.8: FEA prediction of propagation of the crack using a node-release method as viewed at the free surface. At a load of 1,350 N, the crack-induced stress concentration moves past the particle; subsequently, a partial strain decrease is predicted.

must be identified. The general framework for the parameter identification of the SMA particle was developed by Whitten and Hartl and uses the Python programming language to combine Abaqus FEA analysis with a variety of other program libraries [75]. In particular, it utilizes open-source SciPy (Scientific Python) [29] optimization algorithms to minimize the error between experimental and simulated surface strain field results.

The framework is shown in Figure 3.9 and requires three inputs: a temporally varying experimental in-plane strain data over some surface subdomain (obtained from DIC results), an associated FEA model outputting results for the same domain, and initial guess material parameters and their bounds. The framework iteratively generates and runs the Abaqus analysis with trial model parameters. After each analysis is completed, Python scripts retrieve the simulated strain data at specified points and times and calculates the average strain on the particle face, given by

$$\hat{\boldsymbol{\varepsilon}}^{sim} = \frac{1}{A}\int \boldsymbol{\varepsilon}^{sim}(x,y)\mathrm{d}A \approx \frac{1}{A}\sum_{i=1}^{n} \boldsymbol{\varepsilon}_i^{sim} a_i, \tag{3.2.4}$$

$$\boldsymbol{\varepsilon}^{sim} = \{\varepsilon_{xx}^{sim}, \varepsilon_{yy}^{sim}, \varepsilon_{zz}^{sim}\}^T, \tag{3.2.5}$$

where A is the exposed surface area of the particle, n is the number of nodes on the particle face, and a_i is the surface area associated with the data point a_i[2]. The framework then calculates the error between $\hat{\boldsymbol{\varepsilon}}^{exp}$ and $\hat{\boldsymbol{\varepsilon}}^{sim}$. After each simulation, the minimization algorithm produces a new set of trial model parameters based on the total error until the error is minimized. The optimized material parameters are then returned. Thus, the optimization problem becomes

$$\mathbf{s*} = \arg\min[\epsilon(\mathbf{s})], \tag{3.2.6}$$

where $\mathbf{s*}$ is the set of optimized material parameters and ϵ is the strain error given by

$$\epsilon(\mathbf{s}) = \sum_{i=1}^{p}(\|\hat{\boldsymbol{\varepsilon}}_i^{exp} - hat\boldsymbol{\varepsilon}_i^{sim}(\mathbf{s})\|)^2, \qquad \mathbf{s} = \{E_A, M_s, M_s - M_f, H\}, \tag{3.2.7}$$

where p is the number of loading increments (in this work, p=29).

3.3 Material Property Calibration

Table 3.2 shows the bounds and initial parameters for each material property considered. A brief discussion regarding the derivation of the parameter bounds is necessary to understand the findings of this study. The bounds for E_A are based on the austenitic modulus of NiTi wires [61] (lower bound) and bulk NiTi specimens [26] (upper bound). The bounds for M_s were determined by estimating values that would allow the particle to remain in the austenite phase throughout loading (lower bound) or immediately transform at the beginning of loading (upper bound) while

[2]Given the uniformity of the particle mesh, we will assume that each point has the same surface area a_i. Thus, we have simply $\hat{\boldsymbol{\varepsilon}}^{sim} \approx \frac{1}{n}\sum_{i=1}^{n}\boldsymbol{\varepsilon}^{sim}$.

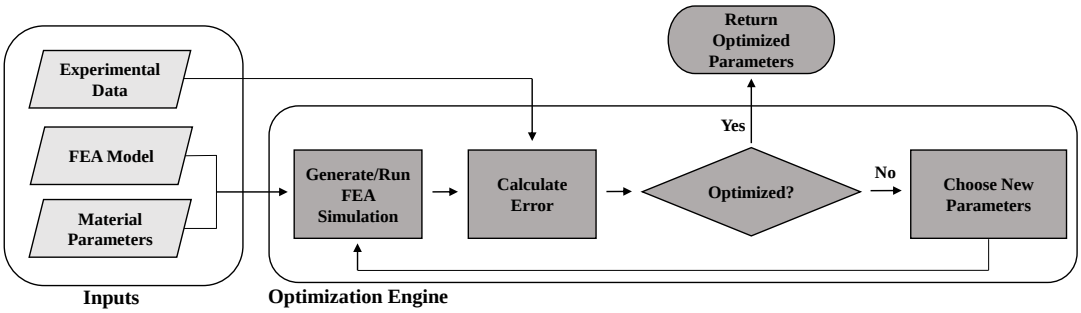

Figure 3.9: Flowchart of the parameter identification framework.

also ensuring that the particle begins in the austenite phase. The considered parameter $(M_s - M_f)$ was necessarily positive but bounded so as to provide reasonable transformation hardening. The lower bound for the transformation strain H represents the possibility that processing may have almost eliminated the pseudoelastic response of the particle completely. The upper bound is based on numerous experimental tests that show NiTi exhibits a maximum possible transformation strain of around 8% [26].

Table 3.2: Initial property values and bounds used during optimization. Note that the ambient temperature is 298 K.

Parameter	Lower Bound	Upper Bound	Initial Guess
E_A (MPa)	50,000	100,000	75,000
M_s (K)	248	296	278
$M_s - M_f$ (K)	35	5	15
H	1.0%	7.5%	3.0%

3.3.1 Material Property Trends

A three-level full-factorial design of experiment (DOE) study was conducted considering sensory particle transformation properties. This study involved considering each property at three different levels for a total of $3^3 = 27$ analyses (Table 3.3) to expand the quantitative and qualitative understanding of the effect each property has on particle response. For each simulation, the load at which particle transformation initiated (a specimen global result), the strain error between the experimental and FEA results (a particle surface result; Equation 3.2.6), and the amount of average martensitic transformation that occured (a particle volume result) was recorded.

Table 3.3: Parameter values for the design of experiment (DOE) study. Values correspond to the optimization bounds of Table 3.2 with the exception of the lowest value of M_s, which was increased to ensure transformation occurs during loading.

Level	-1	0	1
M_s (K)	258	278	296
$M_s - M_f$ (K)	5	15	35
H	1.0%	3.0%	7.5%

Figure 3.10a shows the effect of each parameter on the load at which particle transformation initiates. As discussed above, at the lower bound of M_s transformation initiates only at the end of loading, while at the upper bound transformation initiates soon after loading begins. As expected, $M_s - M_f$ and H have no effect on the onset of transformation. Figure 3.10b shows that the simulation strain error relative to experimental predictions increases as H increases. Increasing M_s and $Ms - M_f$, on the other hand, causes a decrease in strain error. It is also interesting to note

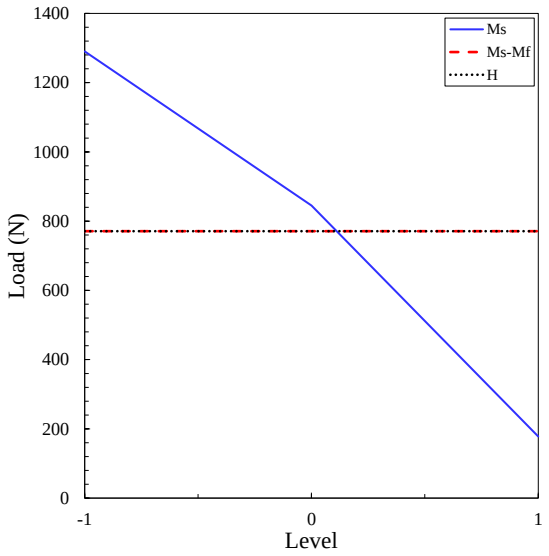

(a) Load at which particle transformation initiates.

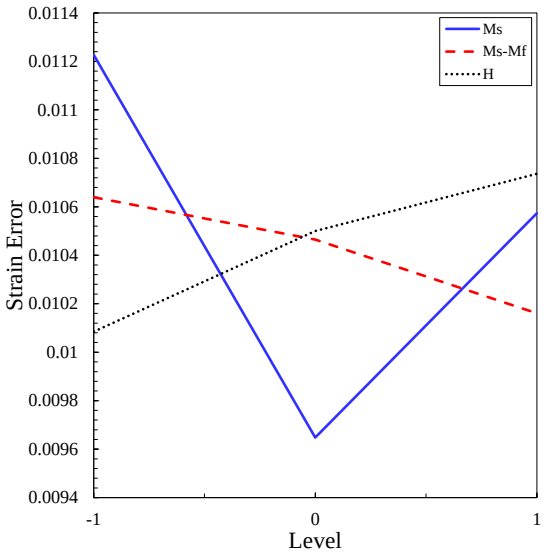

(b) Error between experimental and simulated results.

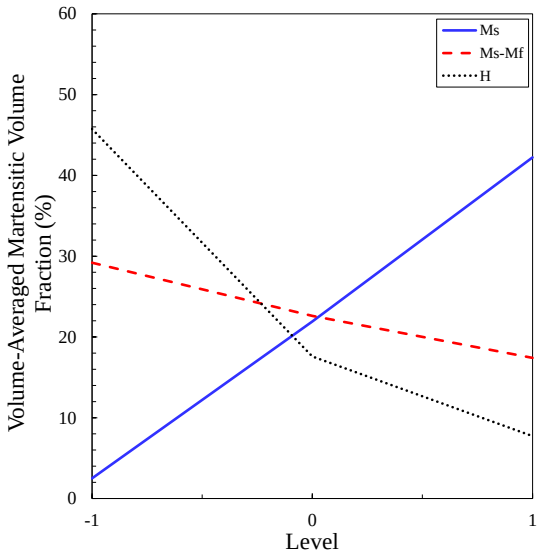

(c) Volume-averaged martensitic transformation in the particle at the end of loading.

Figure 3.10: Factor effects plots associated with the DOE study showing the influence of M_s, $(M_s - M_f)$, and H.

that M_s has a much stronger effect on the resulting error than $M_s - M_f$ or H.

To quantify the amount of transformation occuring in the particle, and thus the sensitivity of the SMA particle as a transformation-based sensor, the volume-averaged *martensitic volume fraction* (MVF) $\hat{\xi}$ was calculated as

$$\hat{\xi} = \frac{1}{V} \int \xi(x, y) \mathrm{d}V \approx \frac{1}{V} \sum_{i=1}^{n} \xi_i V_i, \tag{3.3.8}$$

where $\xi(x, y)$ is the local continuum MVF value, ξ_i and V_i are the MVF and volume at the i^{th} integration point, respectively, n is the number of integration points in the particle volume, and V is the total volume of the particle. Note that V_i is an output provided by the Abaqus post-processor. Figure 3.10c shows the effects of each parameter on the MVF at the end of loading, which can be quite high for the loading conditions and particle configuration considered. Notice that as M_s increases, the MVF in the particle also increases. This agrees with the results in Figure 3.10a, as increasing M_s causes transformation to initiate earlier, leading to more advanced martensitic transformation overall. Increasing $M_s - M_f$ causes a decrease in martensite generation, which is intuitive given that it will take a larger amount of stress to cause complete transformation. However, to generate greater amounts of martensite and therefore a greater magnitude of the detected response, a low maximum transformation strain value H is desired. In this way, SMA bodies for sensory applications differ from SMA components used as actuators, where in the latter high transformation strains are desired to produce greater amounts of recoverable deformation and this greater actuation work. Future studies might exploit this effect to tune the material properties of the sensory particles to emit greater detectable responses.

3.3.2 Optimization Results

The experimentally measured data, FEA model with node-release crack propagation approximation (cf. Section 3.2.1), and known/assumed material parameters were then input into the optimization framework discussed above and shown in Figure 3.9 for the purpose of finding best estimates of SMA particle properties. The optimization framework utilized the Limited-memory Broyden-Fletcher-Goldfarb-Shanno Bounded (L-BFGS-B) optimization algorithm provided in SciPy, which is a quasi-Newton method that has shown good performance for constrained non-smooth optimization [51]. Each iteration featured a parameter step size of 5% for estimating local gradients of ϵ, and convergence occurred after 118 iterations. Table 3.4 shows the optimized values for each property, while Figure 3.11 shows a comparison between the experimental data and simulated results using both the initial parameters and optimized parameters[1]; comparing the evolution of $\hat{\varepsilon}_{yy}$ predicted using the optimized parameters with that of the initial values, it is evident that the optimization leads to a better overall fit with the experimental data. Figure 3.12 shows that crack propagation causes a predicted martensitic transformation of over 50%, which is promising in terms of using these particles for sensing based on phase transformation.

3.4 Damage Model

To more rigorously simulate damage and potential crack propagation in the specimen during loading without resorting to the node-release approximation, the ductile damage model described in Section 2.2.3 is added to the region surrounding the sensory particle. As discussed in Section 3.2.1, the incorporation of damage variables

[1]Note that the internal fields predicted by the finite element model are non-uniform, which disagrees with the findings of Eshelby's inclusion problems [19]. However, these problems consider an elastic inclusion in an infinite elastic body; in the model, both the SMA particle and surrounding matrix have non-linear responses, so these non-uniform internal fields are to be expected.

Table 3.4: Property values determined during optimization.

Parameter	Optimized Result
E_A (MPa)	100,000
M_s (K)	293.0
$M_s - M_f$ (K)	34.80
H	1.327%

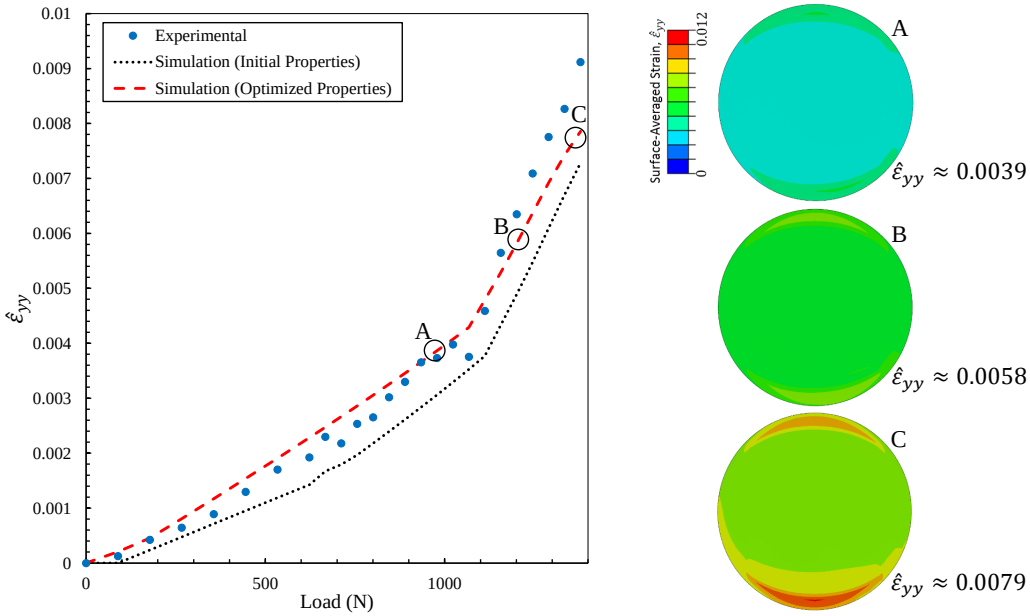

Figure 3.11: Predicted $\hat{\varepsilon}_{yy}$ as a function of applied load using the optimized material properties compared with experimental results and results with initial properties used by the optimization framework. Also shown are contour plots of $\hat{\varepsilon}_{yy}$ on the particle face.

into the FEA model is computationally expensive and was not used for iterative parameter identification[2]; it is introduced here to ensure that our optimized param-

[2]In testing the damage modeling and node release approaches, it was found that a single node release analysis required 1.5 hrs while a similar analysis performed using the continuum damage modeling required $\sim$ 2 days.

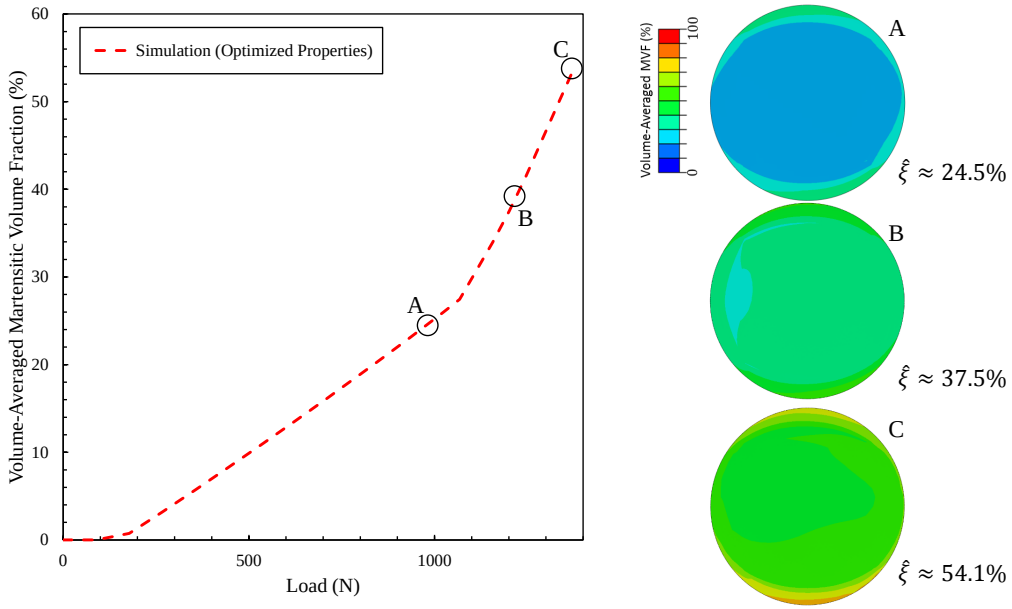

Figure 3.12: Volume-averaged MVF $\hat{\xi}$ as a function of applied load, along with contour plots of the MVF on the particle surface. Transformation initiates when loading reaches 200 N.

eters remain valid for more realistic (i.e. three-dimensional) crack propagation. The data needed to formulate the damage initiation criterion for the particular aluminum system considered in this work was not acquired during the experiment, so data from an alternative aluminum system was used (cf. Appendix C) [71]. For this study, the fracture energy per unit area is G_f=0.4 $\frac{\text{kJ}}{\text{m}^2}$, which is below experimentally measured values but was found to ensure sufficient damage to simulate crack propagation. It has been hypothesized that material processing and/or initial fatigue cycling may have weakened the aluminum matrix.

Figure 3.13 shows the crack propagation along the negative y-surface predicted by the previous node-release model and updated matrix damage model. The crack profile predicted via damage modeling (bottom) is more representative of those seen in

experiments than the incremental node-release approximation (top) used previously, especially with regard to the expected crack tunneling behavior [38]. However, the damage model fails to predict crack propagtion along the free surface of the specimen, which was seen in the experiment; this is due to equivalent plastic strain predictions failing to reach reach magnitudes necessary to induce material degredation. Figure 3.14 shows $\hat{\varepsilon}_{yy}$ as a function of load for the experiment, the previous node-release model, and the aluminum damage model. The divergence from a linear response near 500 N is indicative of crack propagation. At a load of around 1,400 N a decrease in $\hat{\varepsilon}_{yy}$ in the particle is predicted by the damage model. By this point the crack is predicted to have propagated past the particle, leaving the particle behind the damage zone. However, the true experimental final failure mechanism of Figure 3.4 is not modeled here. Figure 3.15 shows the volume-averaged MVF predicted by both models, indicating that the particle may reach nearly 70% martensitic state at the end of loading when damage is considered. The stagnation of transformation at the end of loading can once again be explained by the conservative prediction of crack propagation past the sensory particle. These results show that our optimized material properties of Table 3.4 are reasonable and that the modeling of actual damage and associated crack propagation in the host aluminum leads to more accurate predictions.

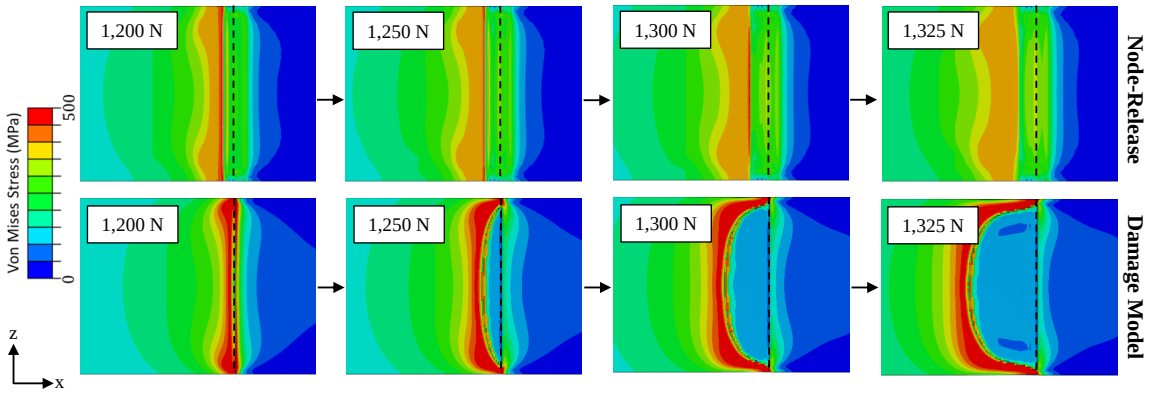

Figure 3.13: Crack propagation predicted using the implemented ductile damage model (bottom) compared with crack propagation using the node-release method (top). Dashed black lines show the position of the crack tip before loading. The damage model exhibits a predicted crack profile closer to those observed during experimental testing (i.e. strong tunneling effect in the specimen) [38].

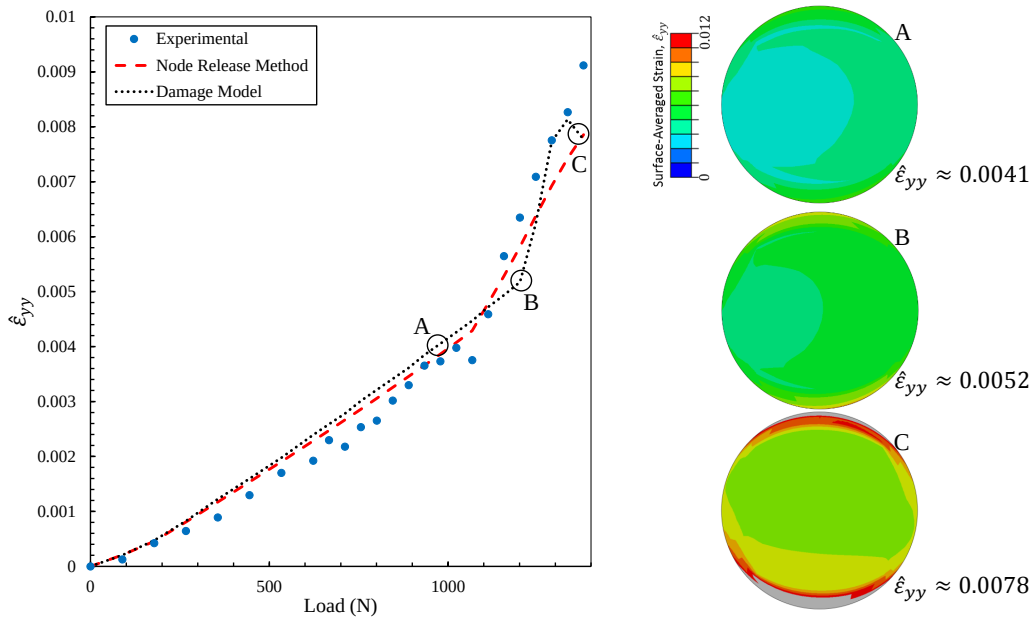

Figure 3.14: Predicted $\hat{\varepsilon}_{yy}$ as a function of applied load using the implemented damage model and a comparison of both experimental strain data and predicted strains using a node-release technique, along with contour plots of $\hat{\varepsilon}_{yy}$ on the particle face.

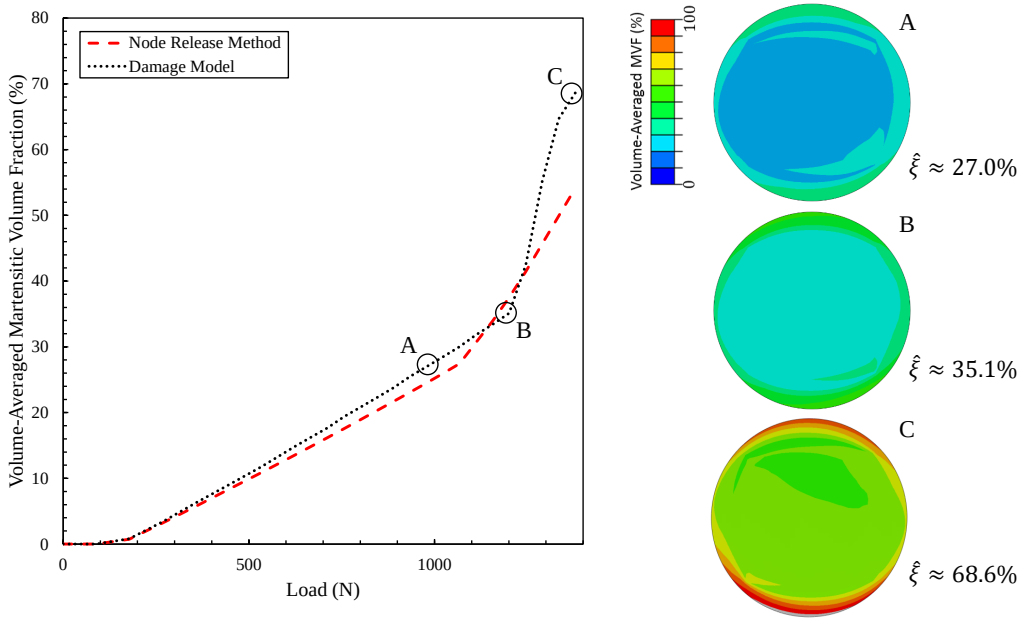

Figure 3.15: Volume-averaged MVF as a function of applied load for the damage model and comparison of predicted MVF using a node-release technique, along with contour plots of the MVF on the particle face.

4. COMPUTATIONAL ASSESSMENT OF SMA SENSORY PARTICLE-BASED CRACK LOCATION IN AIRCRAFT STRUCTURE VIA SUBSTRUCTURE MODELING

We now shift our focus to visualizing a potential engineering application of this damage detection method: an aircraft wing with SMA particles embedded in a rib near structural damage. This problem will further demonstrate this technique as well as examine the effect of particle position relative to a propagating crack on particle response. However, since an aircraft wing is a complex structure spanning dozens of meters and containing multiple parts, an associated finite element model must consider hundreds of thousands of elements; full analysis of such a model, when also considering the highly non-linear behavior of the SMA sensory particles and crack propagation via XFEM, could quickly become computationally infeasible. To address this issue, the finite element model here makes use of substructure modeling (cf. Section 2.3.1), which retains degrees of freedom only at specified points in a model [71]. The chapter will then seek to expand upon this damage detection method by demonstrating that sensory particle response can be used to not only detect the presence of structural damage, but also approximate its location. This is achieved by radial basis function interpolation (cf. Section 2.4.2), which uses particle response to approximate a stress field and locate areas of high stress.

4.1 Computational Model

The finite element model of the aircraft wing was developed in the Abaqus finite element suite using files associated with the Common Research Model (CRM). The CRM is a NASA program developed to create a benchmark model for the validation of specific components of computational fluid dynamic programs [11, 33, 58]. The

wing is based on a transonic commercial transport configuration designed to operate at a cruise Mach number of $\mathrm{M} = 0.85$ with an aspect ratio of $\mathrm{AR} = 9.0$, a taper-ratio of $\lambda = 0.l275$, a span of 58.76 m (2,313 in), and a gross vehicle weight of around 226,800 kg (500,000 $\mathrm{lb_m}$). These specifications closely resemble those of a Boeing 787-8. The structure consists of an elastically-isotropic aluminum with an elastic modulus of $\mathrm{E} = 70{,}000$ MPa (10,000 ksi), a Poisson's ratio of $\nu = 0.32$, and a mass density of $\rho = 2768\,\mathrm{kg/m^3}$ ($0.1\,\mathrm{lb_m/in^3}$) [70].

For the duration of this study, the wing is assumed to be subject to an elliptical loading distribution, with forces applied directly to the main spar of the wingbox. To that end, a local coordinate system is defined with its origin located at the intersection of the main spar with the root rib of the wingbox, with its x-axis oriented along the length of the spar (denoted x') (Figure 4.2). This elliptical loading distribution is approximated by applying a concentrated force f_i to a each node along the spar as position x'_i with magnitude

$$f_i(x'_i) = \int_{x'_i}^{x'_{i+1}} \frac{2W}{\pi L} \sqrt{1 - \left(\frac{x'}{L}\right)^2}\, \mathrm{d}x' \tag{4.1.1}$$

where W is the weight of the aircraft[1], L is the length of the span, and x_i is the distance from the origin to the node in question. It can be shown from this equation that a single wing is subjected to a combined load of $W/2$.

4.1.1 Substructure Implementation

Generally, substructures are utilized to model smaller parts of a larger overall model. However, as discussed in Section 2.3.1.2, the nonlinear behavior of the SMA

[1]In this study, we reduce this weight to the maximum zero-fuel weight of a Boeing 787-8 (161,000 kg or 355,000 $\mathrm{lb_m}$) (cf. [58]) and neglect the weight of the engine (approximately 5,600 kg or 13,000 $\mathrm{lb_m}$) as well as the structural weight of the wing itself (approximately 11,500 kg or 25,200 $\mathrm{lb_m}$). Thus, at 1 G the wing experiences a total lifting force of approximately 625,000 N (140,000 $\mathrm{lb_m}$).

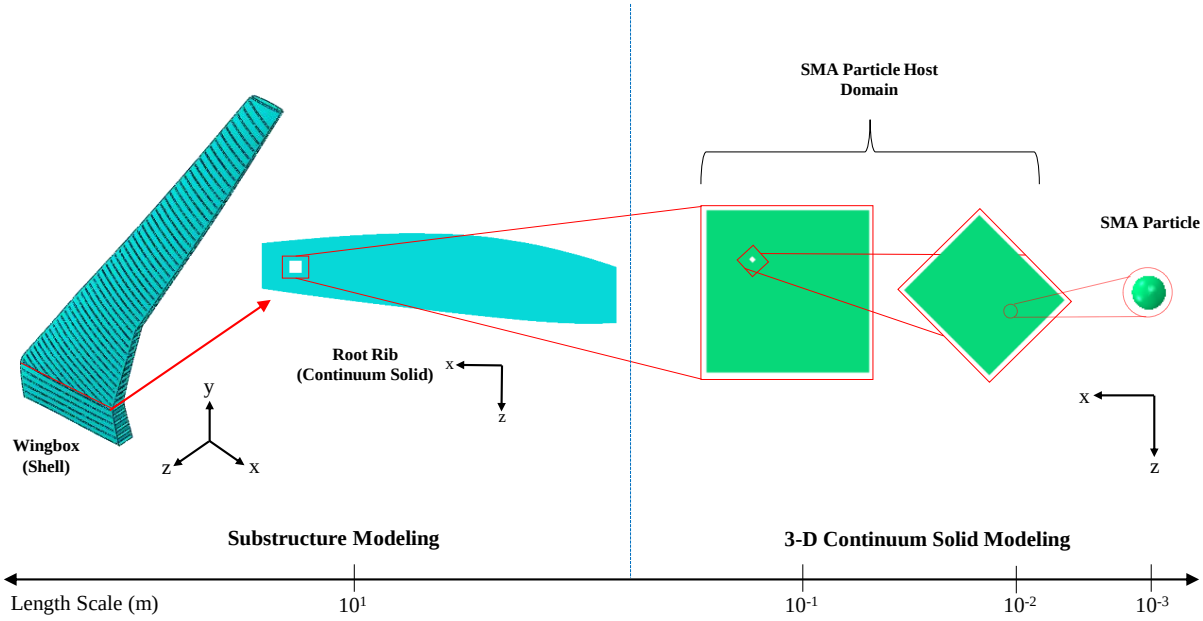

Figure 4.1: Assembly of the wingbox using a combination of substructure and solid modeling.

sensory particles (the smallest body considered herein) is not compatible with substructure domains. Therefore, in this work an alternate approach is considered. Substructure modeling is used to transition from a large scale structure (the full wing) to small scale parts (SMA particles). The wingbox and a majority of the root rib are designated as substructures, while a small section of the rib is modeled using 3-D continuum solid elements. The entire model assembly is shown in Figure 4.1. The modeling of each part will be further discussed in the next section.

4.1.2 Wingbox Substructure

The pre-meshed CRM model structure consists of 57,292 linear shell elements with reduced integration, corresponding to 52,393 nodes and 314,358 total DOFs.

The large number of variables that must be considered in this model, coupled with the objective of transitioning across length scales to perform computationally efficient detailed studies on a small area, make it a perfect candidate for substructure modeling. For ease of implementation, the root rib is removed from the wingbox prior to substructure generation; its reattachment will be discussed in Section 4.1.3. For the wingbox substructure, nodes are retained

1. Along the negative y-surface of the wingbox, for the application of boundary conditions,

2. At points along the chord of the wingbox where the root rib intersects spars and longerons, for reattachment of the root rib,

3. Along the positive z-edge of the main spar, for the application of loads.

Thus, the substructure contains 6,366 DOFs (Figure 4.2), or a reduction of approximately 98% from the original wingbox model with the root rib removed.

4.1.3 Root Rib Substructure

As mentioned previously, the root rib of the wingbox is a separate substructure model. The rib is 7.366 m (290 in) long, and is partitioned along axes where the root rib is intersected by spars and longerons from the wingbox substructure. A small square with dimensions 254 $\times$ 254 mm (10 $\times$ 10 in) is removed from an arbitrary portion of the rib free from such intersections and in an area of high stress; this domain is where the SMA sensory particles will be embedded and damage will be added to the rib. It is important to mention that while the original root rib in the CRM model consisted of shell elements, this rib is constructed using 3-D continuum solid elements with a total rib thickness of 6 mm (0.24 in). This modification is required to ensure a proper tied interface with the domain containing the sensory particles, which

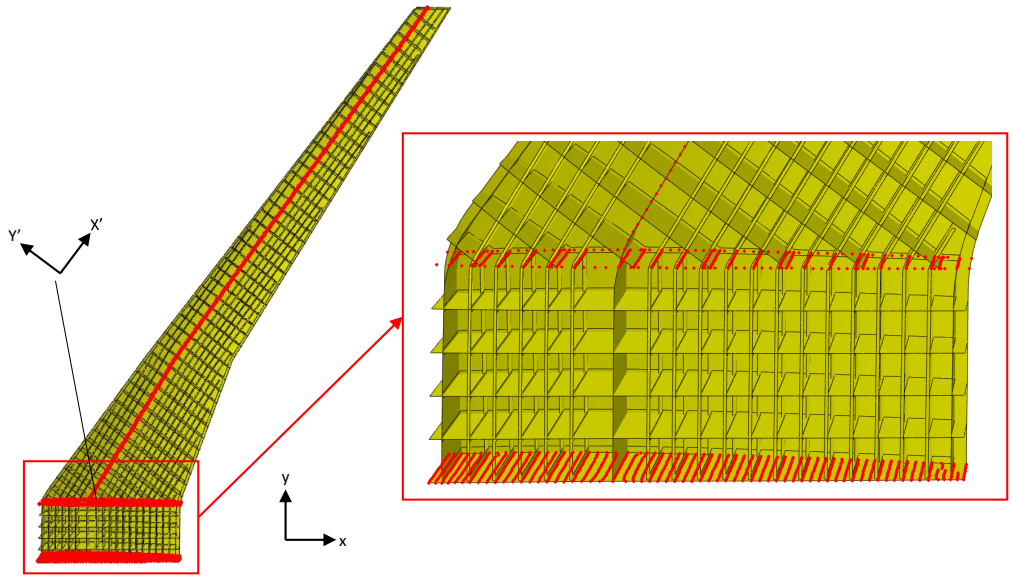

Figure 4.2: Retained DOFs associated with the wingbox substructure.

cannot be modeled using shell elements. The rib consists of 3,760 linear elements with reduced integration, corresponding to 23,514 DOFs. In an attempt to remain consistent with the original CRM model, the mesh on the rib substructure remains relatively coarse. As with the wingbox, this root rib is generated as a substructure to further improve computationally efficiency as well as demonstrate the ability of substructures to bridge multiple length scales. Nodes on the rib are retained

1. Along axes where the root rib is joined with the wingbox substructure

2. Along edges where the SMA particle host domain will be connected to the rib substructure

The generation of a root rib substructure results in 6,750 retained DOFs (Figure 4.3), which is a reduction of nearly 71% relative to a continuum-solid root rib not designated as a substructure. However, the original CRM shell-based rib contains 5,853

DOFs, so a slight increase in variables is incurred to ensure a proper tied interface with the sensory particle host domain.

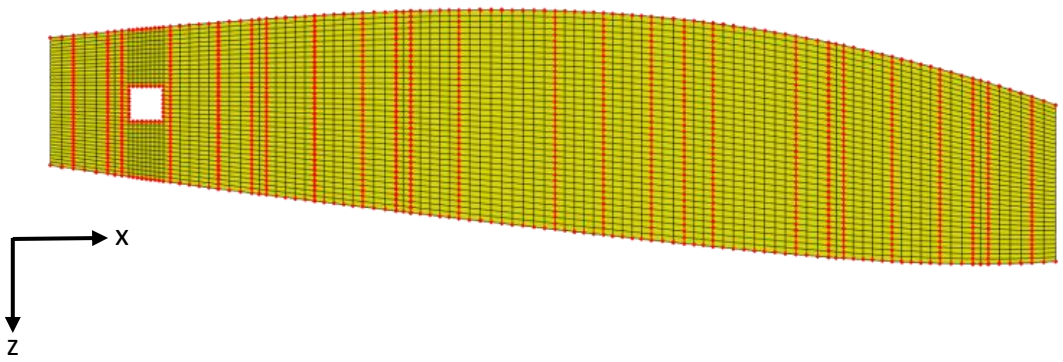

Figure 4.3: Retained DOFs associated with the root rib substructure.

The root rib substructure (Figure 4.3) is reattached to the wingbox substructure (Figure 4.2) via tie constraints in Abaqus. Prior to sensory particle analysis, tests were conducted to ensure that the change to a solid element root rib has a minimal effect on the stress field in the rib. Figure 4.4 shows that the stress fields generated in the solid rib are relatively consistent with the original shell-based rib, and that the tie constraint is behaving as expected.

4.1.4 Sensory Particle Host Domain

To simulate a series of SMA sensory particles embedded in the root rib, a smaller nested structure is created. This structure consists of a square with dimensions 254 x 254 mm (10 x 10 in) and a rectangle with dimensions 7.5 x 5 mm (0.3 x 0.2 in) (Figure 4.5). The sensory particles reside in the smaller domain, and will be discussed in detail in Section 4.1.5. These nested domains consist of an isotropic aluminum

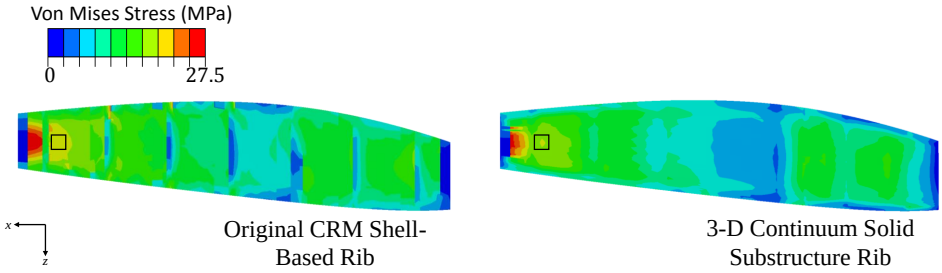

Figure 4.4: Comparison of local stress field results experienced by the shell-based and solid-based ribs when the wing is loaded to 1 G. The location of the sensory particle host domain is shown by the black box. The solid rib captures the response of the shell-based rib while also providing a better transition to the solid-element particle host domain.

with the same properties as the wingbox and root rib substructures. Because tie constraints allow for rapid mesh transitions between parts, the smaller domain is tied to the interior surface of the larger domain, which in turn is joined to the rib substructure.

In this study, two different cases are considered. The first case considers a structure free from any structural damage or defects (i.e. no stress concentrations). This is used to establish a baseline for the response of the SMA particles to loading. The second case considers the particles' response to a propagating crack. To this end, a precrack of length 33 mm (1.3 in) emanating from a hole of radius r=38 mm (1.5 in) towards the sensory particles, is introduced into the host domain. The crack is allowed to propagate using the XFEM method discussed in Section 2.3.2. This is implemented in the model by specifying a maximum principal stress of 200 MPa (30,000 psi) and a fracture energy of 0.0109 MPa·m (60 psi·in) in the larger housing [34].

As will be discussed in Section 2.3.2, this implementation of damage used herein

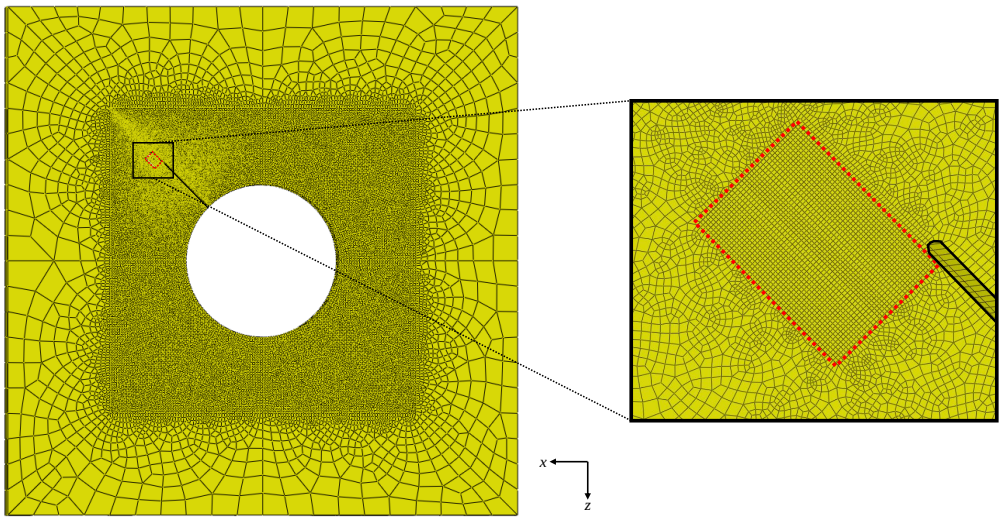

Figure 4.5: Assembly of the sensory particle host domain using tie constrains (denoted by dashed lines).

requires a refined mesh to eliminate mesh dependency. This refined mesh has the added benefit of facilitating consistent crack propagation, as the crack must propagate across an entire element at a time. Each part consists of linear elements with reduced integration, with a combined total of 206,549 elements (including the SMA sensory particles) (Figure 4.5). It is important to note that while the overall size of the problem has increased, the use of substructure modeling allows for the efficient relation between the globally-applied loads and local structural response.

4.1.5 SMA Sensory Particles

The six SMA sensory particles considered herein are of radius r=500 μm (0.02 in) with material properties given in Table 3.1 and Table 3.4. The behavior of these particles is governed by a numerical representation of the SMA model discussed in Section 2.2.2 [36]. For this study, a nominal temperature of 298 K is applied to each

each particle. Figure 4.6 depicts the constitutive relationship between local stress and local MVF, which corresponds to the magnitude of the response exhibited by the particle, at this temperature. Note that by varying the temperature by 4 K in either direction, the transformation behavior of the SMA changes. This indicates that the response of the SMA particles is dependent on temperature as well as stess, which would need to be taken into accont during any real world engineering implementation of this method.

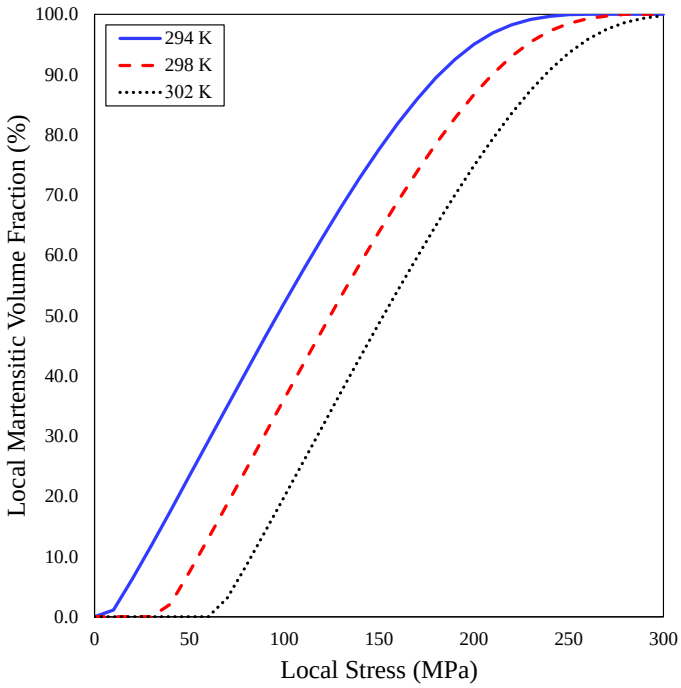

Figure 4.6: Local martensitic volume fraction as a function of local stress for an SMA with material properties given in Table 3.1 and Table 3.4

In an actual application, sensory particles would ideally be spread throughout the volume of a component to "monitor" as much of the structure, as possible given

that the location of structural damage is difficult to predict. However, for the purposes of this numerical demonstration, a particle is placed in an informed location to generate meaningful observations about particle response to damage. To determine an appropriate location of the sensory particle relative to the tip of the precrack, the crack tip stress field equations from the Westergaard solution to Mode I loading are considered [54]. This solution assumes an infinite plate with a crack of length a subjected to biaxial stress σ_o at infinity; while not exactly corresponding to the sensory particle problem addressed in this work, it nevertheless provides useful guidance regarding particle location for this study. The crack tip stress field is given by the following equations:

$$\sigma_{11} = \frac{K_I}{\sqrt{2\pi r}} cos\frac{\theta}{2}\left[1 - sin\frac{\theta}{2}sin\frac{3\theta}{2}\right], \tag{4.1.2}$$

$$\sigma_{22} = \frac{K_I}{\sqrt{2\pi r}} cos\frac{\theta}{2}\left[1 + sin\frac{\theta}{2}sin\frac{3\theta}{2}\right], \tag{4.1.3}$$

$$\sigma_{12} = \frac{K_I}{\sqrt{2\pi r}} cos\frac{\theta}{2}sin\frac{\theta}{2}sin\frac{3\theta}{2}, \tag{4.1.4}$$

$$\sigma_{13} = \sigma_{23} = \sigma_{33} = 0, \tag{4.1.5}$$

where r is the distance from the crack tip, θ is the angle relative to the crack tip, and K_I is the stress intensity factor for Mode I loading, given by

$$K_I = \sigma_o\sqrt{\pi a}. \tag{4.1.6}$$

For this problem, the von Mises stress can be reduced to

$$\sigma = \sqrt{\sigma_{11}^2 - \sigma_{11}\sigma_{22} + \sigma_{22}^2 + 3\sigma_{12}^2}. \tag{4.1.7}$$

Substituting Equations 4.1.2-4.1.4 into Equation 4.1.7, we obtain

$$\sigma = \sqrt{\left(\frac{K_I}{\sqrt{2\pi r}}\right)^2 \cos^2\frac{\theta}{2}\left(1 + 6\sin^2\frac{\theta}{2}\sin^2\frac{3\theta}{2}\right)} \tag{4.1.8}$$

From this equation it can be shown that for a given value of r, the stress is at a maximum when $\theta \approx \pm 67°$.

Figure 4.7 shows a diagram of the placement of each particle. Using the above result, the first particle is embedded 2 mm (0.08 in) away from the precrack tip at an angle of 67°. A second particle is embedded 2 mm above the first along the same 67°-line. This process is repeated at distances of 1.5 mm and 3 mm away from the crack tip along an axis normal to the crack tip.

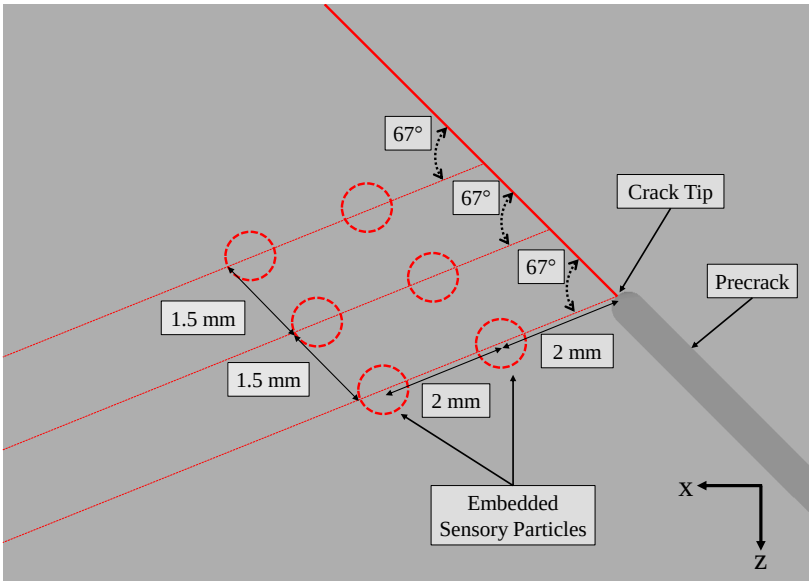

Figure 4.7: Assembly of the sensory particle host domain using tie constraints (denoted by dashed lines).

4.2 Results

The original shell-based CRM model of the wingbox was loaded using the elliptical load distribution discussed in Section 4.1.2. Figure 4.8 depicts the stress distribution over the wing loaded to 1 G, in the positive z-direction. Given the applied ambient temperature and SMA transformation properties (cf. Table 3.1), analysis of particle response during unloading was deemed extraneous to this work. The temperature at which the SMA material considered transforms back into austenite is higher than the applied temperature; the only particle response during unloading is an elastic response, meaning that the amount of martensite generated in the particles at the end of loading will be retained.

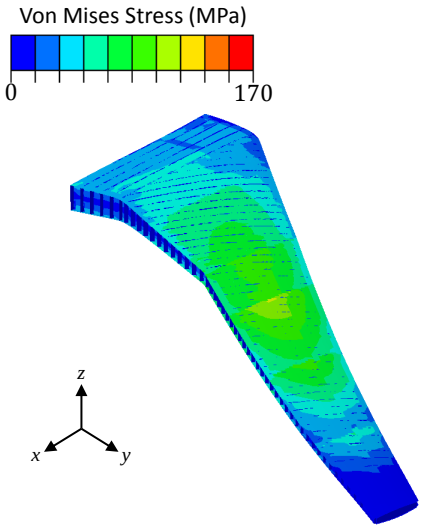

Figure 4.8: Shell-based wingbox loaded to 1 G via the assumed elliptical load distribution applied to the main spar. Note the relatively homogeneous stress distribution in the upper wing skin over much of its span.

The wingbox was assembled using the method discussed in Section 4.1. Lifting loads were applied to the retained nodes along the main spar of the pre-computed wingbox substructure; the global response of the wingbox were then related to the local response of the sensory particles. It is important to note that during loading, the responses of each part (i.e. wingbox, root rib, sensory particles) remain fully coupled. This could allow for substructure modeling to be utilized when analyzing SMA components as actuators, as a change in the local behavior of an actuator could elicit a global response in the overall structure.

The model was then subjected to loading between 0 G and 4 G. These loading conditions are associated with Federal Aviation Regulation commercial aircraft design practices, including basic maneuvering loads (2.5 G) and simplified gust/turbulence loads (3.75 G) [49]. Figure 4.9 shows the propagation of the crack during loading. As the crack began to grow (1 G-2 G), a stress concentration developed around the first sensory particle, initiating phase transformation. However, as loading continued the crack moved past the first particle; while stresses may continue to nominally increase, the rate of transformation in the particle is expected to decrease. As the crack continued to move past the first particle, the associated stress concentration enveloped the second particle, which is expected to continue experiencing phase transformation until the end of loading.

To quantify particle reponse, the volume-averaged MVF, $\hat{\xi}$, was calculated for each particle using Equation 3.3.8. As previously mentioned, this value can be directly related to some magnitude of measurable response (i.e. a change in mageneti-zation in an MSMA). After this calculation, the responses of the sensory particles can be compared to observe meaningful trends. For discussion purposes, each particle is referred to by the numbers designated in Figure 4.10.

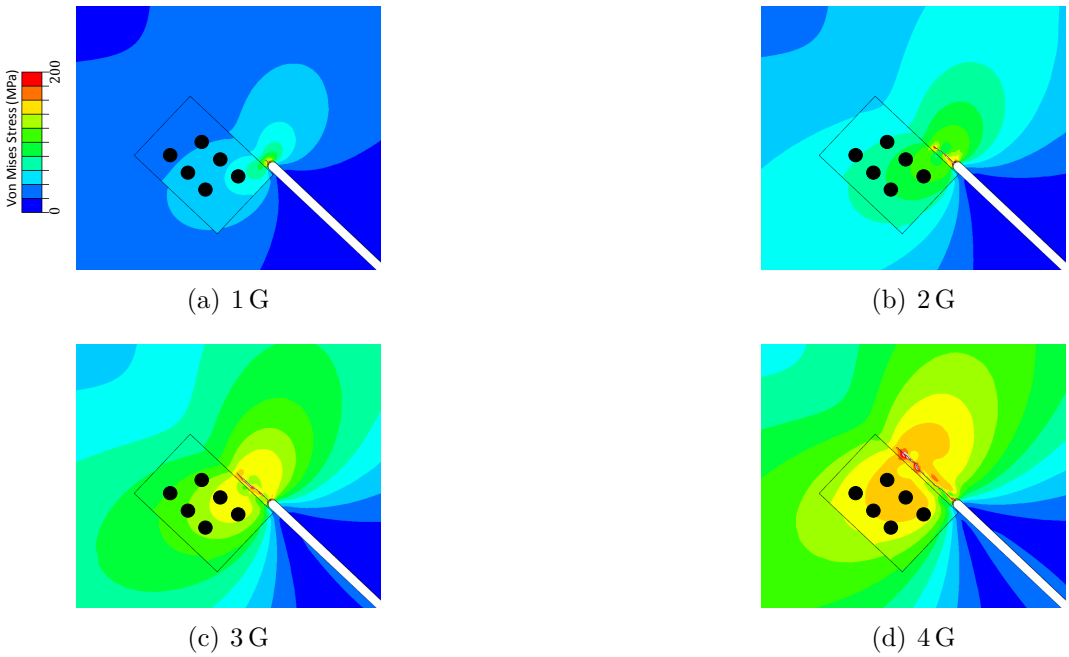

(a) 1 G (b) 2 G

(c) 3 G (d) 4 G

Figure 4.9: Crack propagation and associated stress field evolution during loading. The sensory particles are denoted by the black circles.

4.2.1 Effect of Neighboring Particles on Individual Particle Response

The first analysis considered whether the presence of neighboring sensory particles has any effect on individual particle response. To that end, the problem was analyzed once with all six sensory particles embedded in the root rib and then six times, each with a different individual sensory particle. The results of these simulations are shown in Figure 4.11. As mentioned in Section 2.3.2, crack propagation simulations using XFEM are solution-dependent. This makes comparing different simulations difficult, as crack propagation paths in the particle host domain differed noticeably in several cases. However, notice that in each case the magnitude of the particle response is approximately the same until loads of around 3 G; it is at this load that crack propagation paths began to differ. This result demonstrates that particle

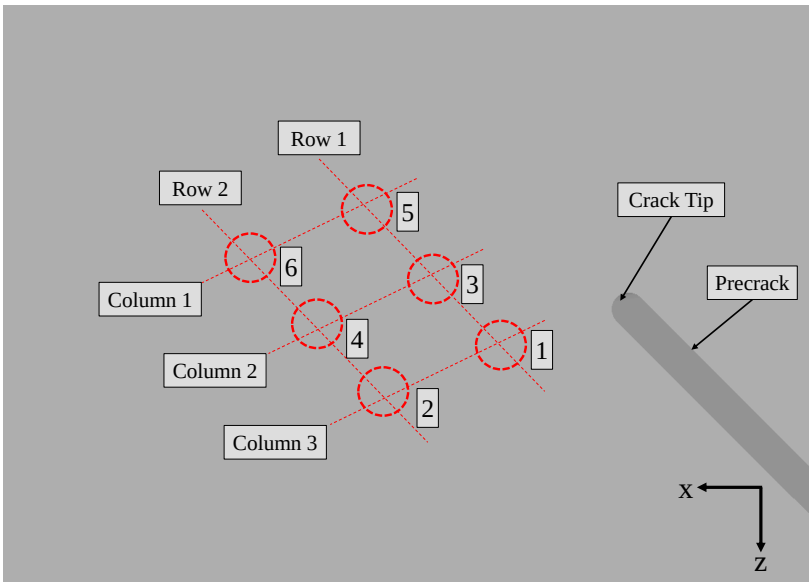

Figure 4.10: Particle notations for discussion purposes.

response is approximately the same regardless of whether there are other sensory particles in the vicinity, allowing for comparison of multiple particle responses from a single simulation. This result also forms the basis of the work that will be presented in Chapter 4.3.

4.2.2 Comparison of Particle Response to Undamaged/Damaged Configurations

The second analysis looked to demonstrate the ability of SMA sensory particles to detect the presence of structural damage. This means ensuring that the sensory particles do not respond similarly to operating loads, thus triggering a "false positiv". A simulation was run with the six sensory particles embedded in an undamaged root rib, with particle responses compared to the responses to crack propagation introduced in Section 4.2.2. Figure 4.12 shows that for each particle the presence of a propagating crack results in a greater magnitude of particle response than that of the same particles embedded in an undamaged component. This result serves to

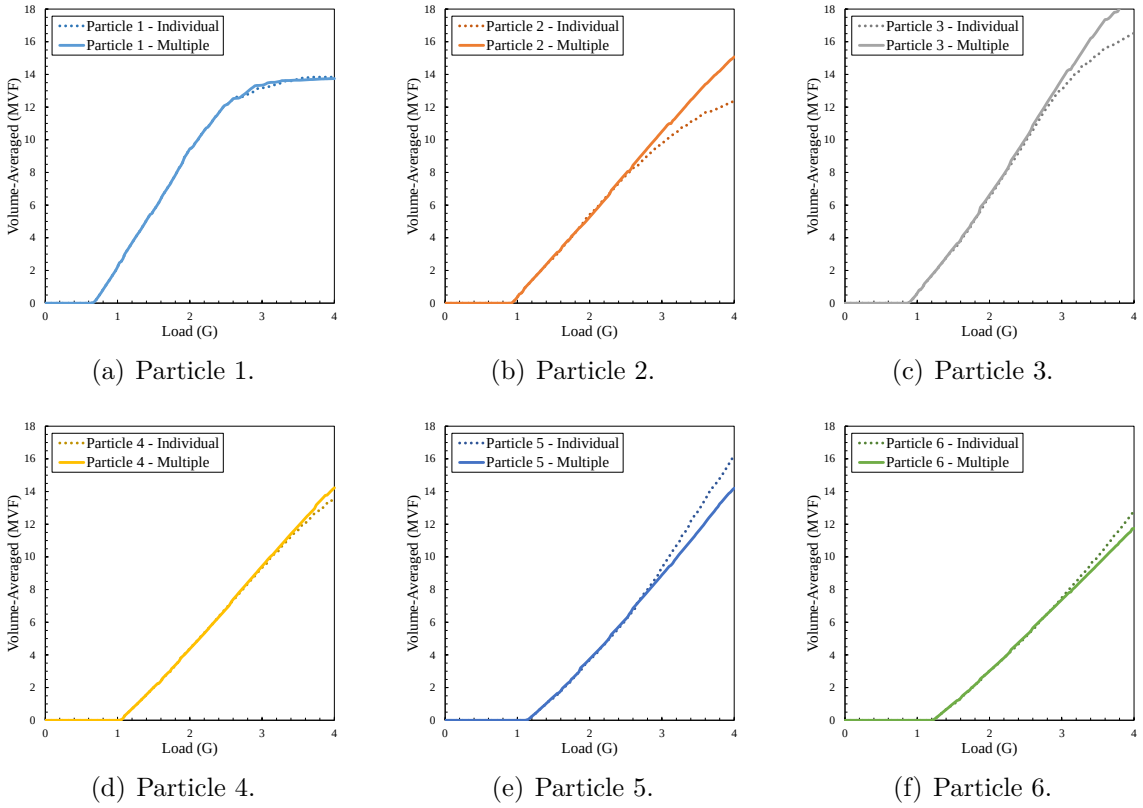

(a) Particle 1. (b) Particle 2. (c) Particle 3.

(d) Particle 4. (e) Particle 5. (f) Particle 6.

Figure 4.11: Comparison of particle response as a function of applied load when considering individual sensory particles and multiple sensory particles.

illustrate the ability of the aforementioned NDE method to detect the presence of structural damage.

4.2.3 Effect of Position Relative to Structural Damage on Particle Response

The final analysis examined how particle response is effected by the location of the particles relative to the crack tip. Because the particles in this problem are structured as an array, particle response can be compared using "rows" (i.e. particles along the same line parallel to the normal of the initial crack tip) and "column" (i.e. particles along the same lines 67° from the normal of the initial crack tip).

Figure 4.13 shows particle response as a function of applied load for each particle

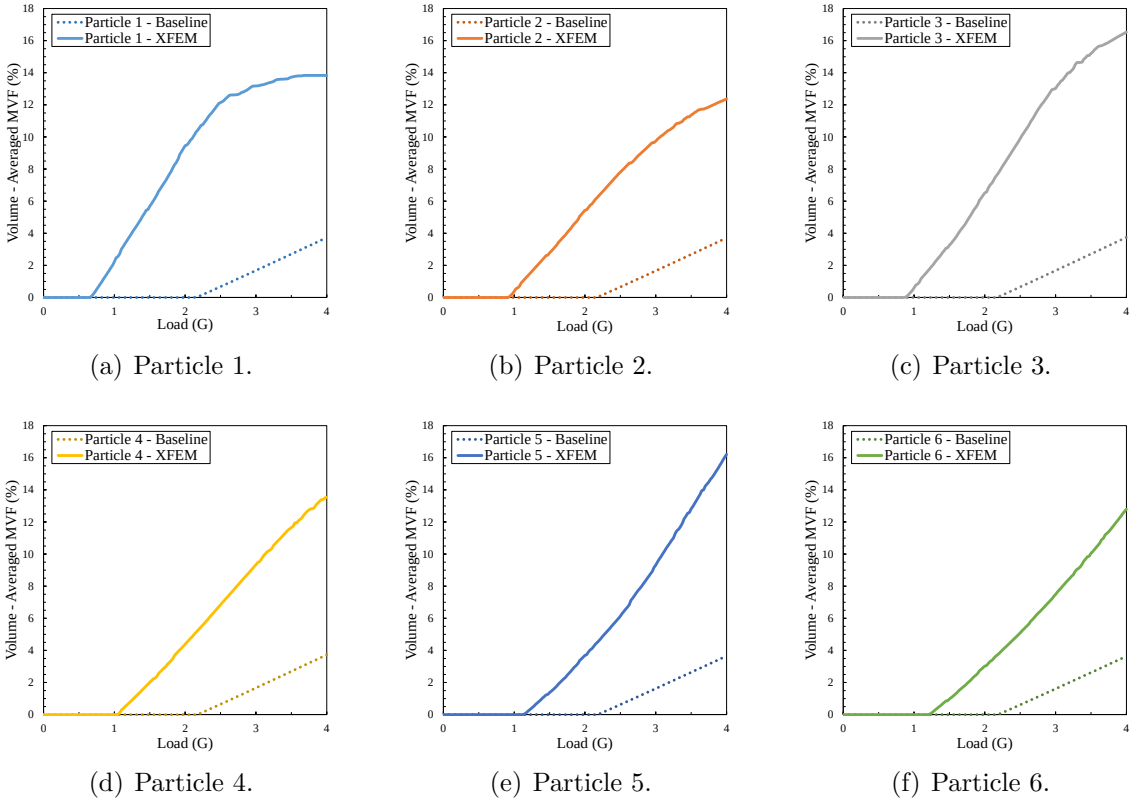

(a) Particle 1. (b) Particle 2. (c) Particle 3.

(d) Particle 4. (e) Particle 5. (f) Particle 6.

Figure 4.12: Comparison of particle response as a function of applied load for the baseline case (i.e. undamaged) and damage case.

row. Note that, as one would expect, the particles closest to the initial crack tip (Particles 1 and 2) experience phase transformation prior to the other particles in their respective rows. However, it is noticeable that the differences in the initiation of phase transformation are less pronounced for the second row (cf. Figure 4.13b). This is perhaps due to the fact that the stress contours further away from the crack tip are less dense, meaning that particles at that distance are experiencing a similar magnitude of stress. Also, it is interesting to note the transformation behavior of the particles as they are enveloped and/or are passed by the stress concentration generated by the crack tip; as a given particle is enveloped by the stress concentration,

the rate of transformation in that particle increases. However, as the crack propagates past a particle the rate of transformation decreases until it reaches a near-constant value. This response is particularly noticeable in Particles 1 and 2, while Particles 3 and 4 also appear to be experiencing the beginnings of this same response at a load of 4 G. Particles 5 and 6 both continue to experience a steady increase in phase transformation since the crack has not yet reached these particles.

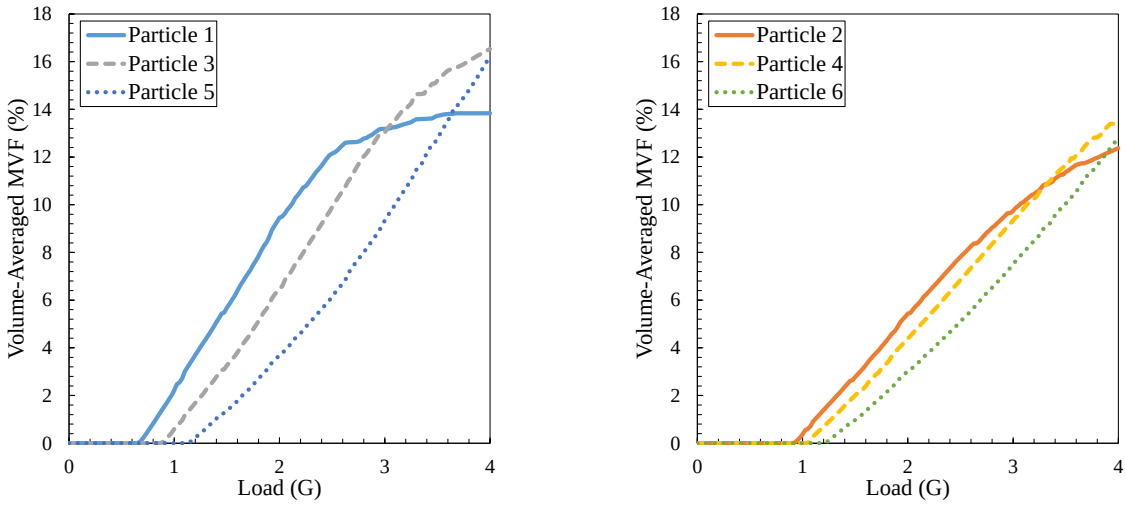

(a) Particle Row 1.

(b) Particle Row 2.

Figure 4.13: Comparison of particle response as a function of applied load during crack propagation for each row of particles.

Figure 4.14 shows particle response as a function of applied load for each particle column. Here, many of the same phenomena can be observed, including the stagnation of phase transformation in particles that have been passed by crack. Once again, it is noticeable that particles closer to the crack experience higher amounts of martensitic transformation. It is also interesting that when far away from the crack, phase transformation in the particles is approximately the same regardless of particle

position (cf. the beginning of loading in Figure 4.14c). This can also be attributed to stress contours far away from the crack tip being less dense.

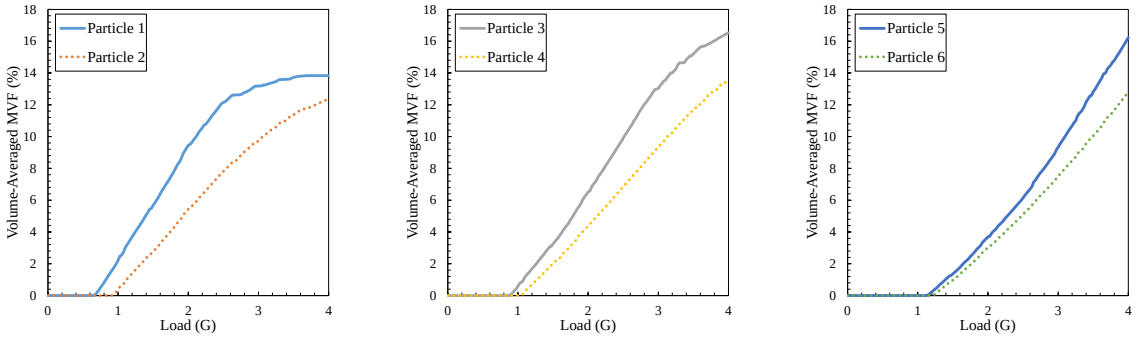

(a) Particle Column 1. (b) Particle Column 2. (c) Particle Column 3.

Figure 4.14: Comparison of particle response as a function of applied load during crack propagation for each column of particles.

4.3 Determination of Crack Tip Location Using SMA Sensory Particles

In the previous section, the phase transformation behavior of SMA sensory particles in the presence of structural damage was demonstrated. Utilizing this behavior could allow for the earlier, and potentially even real-time, detection of fatigue cracks. This section seeks to expand upon this method by focusing on the potential of SMA sensory particles to not only detect the formation of fatigue cracks, but also to approximate the location of such damage. Similar work done by Betz et al. used Lamb wave-detecting fiber Bragg grating in optical fibers and genetic algorithms to approximate the location of small holes in aerospace materials [8]. Here, by relating the amount of martensitic transformation in a given particle to a magnitude of stress via an SMA constitutive model, radial basis function (RBF) interpolation will be used to approximate a potential stress field. Using this approximation, a particle density

study will be conducted to observe how many particles in the vicinity of the crack are needed to accurately locate structural damage using this novel method.

4.3.1 Particle Density Study Formulation

To explore the ability of SMA sensory particles to approximate the location of structural damage, an academic problem (Figure 4.15) was formulated involving 24 sensory particles embedded into the model described in Chapter 4 as shown in Figure 4.16a. For this simulation, the maximum principal stress for XFEM purposes was increased to 485 MPa (70,000 psi); this is to match the experimental elasto-plastic aluminum model in Section 2.2.1. The substructure model was loaded to 4 G, after which the volume-averaged MVF at the end of loading was calculated for each particle (cf. Equation 3.3.8). Recall that Section 4.2.1 demonstrated that particle response is approximately the same regardless of whether there are other sensory particles in the vicinity. Thus, even though the particles described here are not randomly dispersed throughout the structure (as they would be in application), considering a randomly-selected subset of particles from the larger set can simulate such dispersion (cf. 4.16b). This also allows for the consideration of a single crack propagation simulation, avoiding complications from the solution-dependent nature of XFEM seen in Section 4.2.1.

After the crack propagation simulation, the particle density study consists of specifying n number of particles to be considered. A Python script generates a random configuration of n particles and retrieves both the spatial coordinates and volume-averaged MVF of each specified particle. The MVF of each particle is then related to the Mises stress via the SMA constitutive model (cf. Section 2.2.2). Given

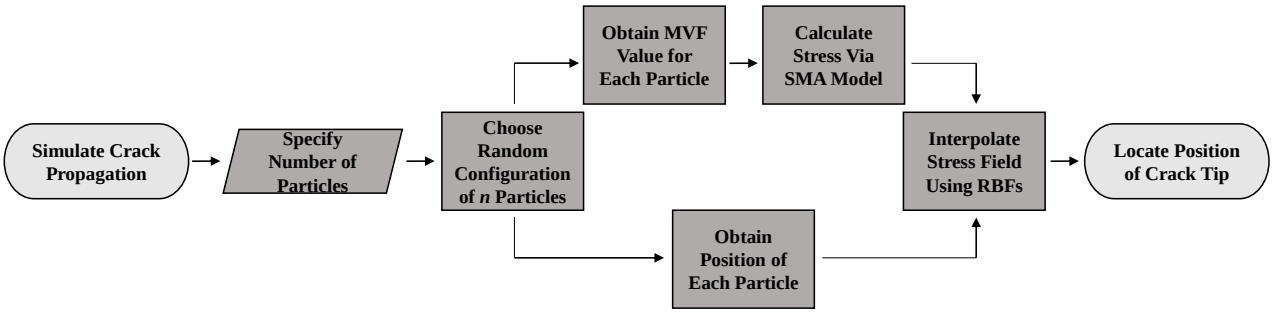

Figure 4.15: Flowchart detailing the particle density study.

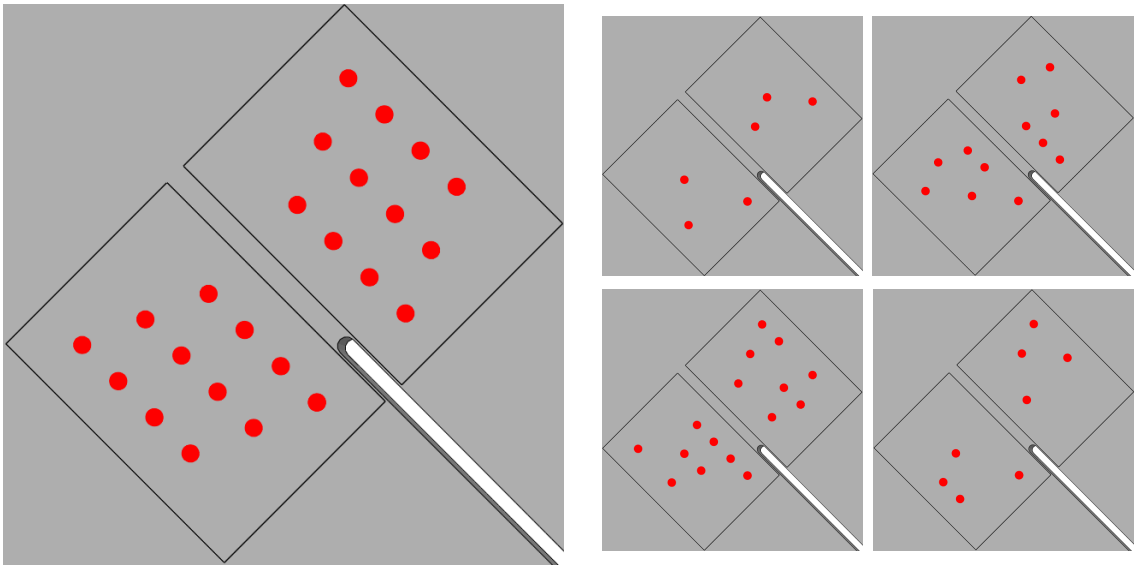

(a) All 24 sensory particles embedded near the pre-crack.

(b) Examples of possible random configurations of particles.

Figure 4.16: Illustration of sensory particles used in the particle density study.

that during transformation $\Phi^t_{fwd} = 0$, Equation 2.2.7 can be rewritten as

$$\bar{\sigma} = \frac{Y + f^t_{fwd}(\xi) + \rho\Delta u_0 - \rho\Delta s_0 T}{H}. \tag{4.3.9}$$

After calculating the Mises stress at each particle, the RBF module included in SciPy and described in [29] is used to interpolate the stress field around the particles (cf. Section 2.4.2).

In this study, a number of assumptions are made. First, it is assumed that the spatial coordinates of each particle are known *a priori*. Second, the SMA particles are assumed to have properties such that they do not reverse transform at operational temperatures and all martensite generated during loading is maintained; this conservation of martensite allows for the particles to maintain the MVF corresponding to the highest applied stress, creating a form of stress field "history". It is also assumed that the magnitude of the measured response of each particle has already been connected to its corresponding MVF value. Finally, it is assumed that the point of highest stress interpolated by the RBFs is the location of the crack tip (in application, a stress singularity forms at the crack tip [54].

4.3.2 Interpolation Results

The study consisted of 20 distinct combinations of n particles (n=4,6,8,...,20). Table 4.1 shows the corresponding particle density and volume fraction for each number of particles. Figure 4.17 shows examples of interpolated stress contour plots for each considered particle density case. For each combination of particles, the location of predicted maximum stress was recorded. Figure 4.18 shows the predicted location of the crack tip for each particle configuration as well as the location of the actual crack tip. Notice that for low numbers of sensory particles in the vicinity of the crack, the predicted crack tip location widely varies. This is because the RBF interpolation is generating the contour with sparse amounts of data. However, as the number of particles increase, the predicted crack tip locations become more precise.

Figure 4.21 shows contour plots of the standard deviation of the interpolated

Table 4.1: Particle density and volume fraction of sensory particles in the interpolation region for each number of particles specified.

Number of Particles	Density (particles/mm^3)	Volume Fraction
4	0.0079	0.4%
6	0.0119	0.6%
8	0.0159	0.8%
10	0.0198	1.0%
12	0.0238	1.2%
14	0.0278	1.4%
16	0.0317	1.6%
18	0.0357	1.8%
20	0.0397	2.0%

stress field for various particle configurations. Note that for lower numbers of particles there are greater amounts of deviation in the interpolated stress because the stress field is much more sensitive to where the particles are located. Considering 12 or more particles results in a notable reduction of deviation in the areas surrounding the sensory particles. The standard deviations in both the x- and y-coordinates, as well as the predicted crack length, are illustrated in Figure 4.20; with a few minor exceptions, the standard deviations of all three components decrease as the number of particles considered increases.

After observing the preciseness of each particle configuration, the accuracy of each configuration was then considered. Contour plots of the average interpolated stress field for various particle configurations are shown in Figure 4.21. Notice the bimodal nature of the interpolated stress contour. Figure 4.22 depicts the average predicted location of the crack tip for each number of particles. As before, low particle densities do not lead to an accurate crack tip approximation, while higher particle densities (here, 10 particles and above) lead to approximations that are within a crack

length of the actual crack tip (0.471 mm). Figure 4.23 shows the average predicted crack tip location, while Figure 4.24 shows difference between this average and the actual crack tip. It is interesting to note that the inclusion of 12 SMA sensory particles yields the most accurate prediction, while the two highest particle density configurations are significantly outperformed by lower particle density configurations. This result, coupled with the result in Figure 4.19c, makes the use of 12 particles, or a sensory particle volume fraction of 1.2% (cf. Table 4.1), the optimal particle density configuration. However, the critical flaw size in a typical aluminum aircraft structure that can lead to catastrophic failure is approximately 63.5 mm (2.5 in) [59]. The least accurate prediction, occuring when considering 4 particles, is still well within safe crack length levels. Therefore, in most cases every particle density configuration considered would be adequate for approximating the location of structural damage.

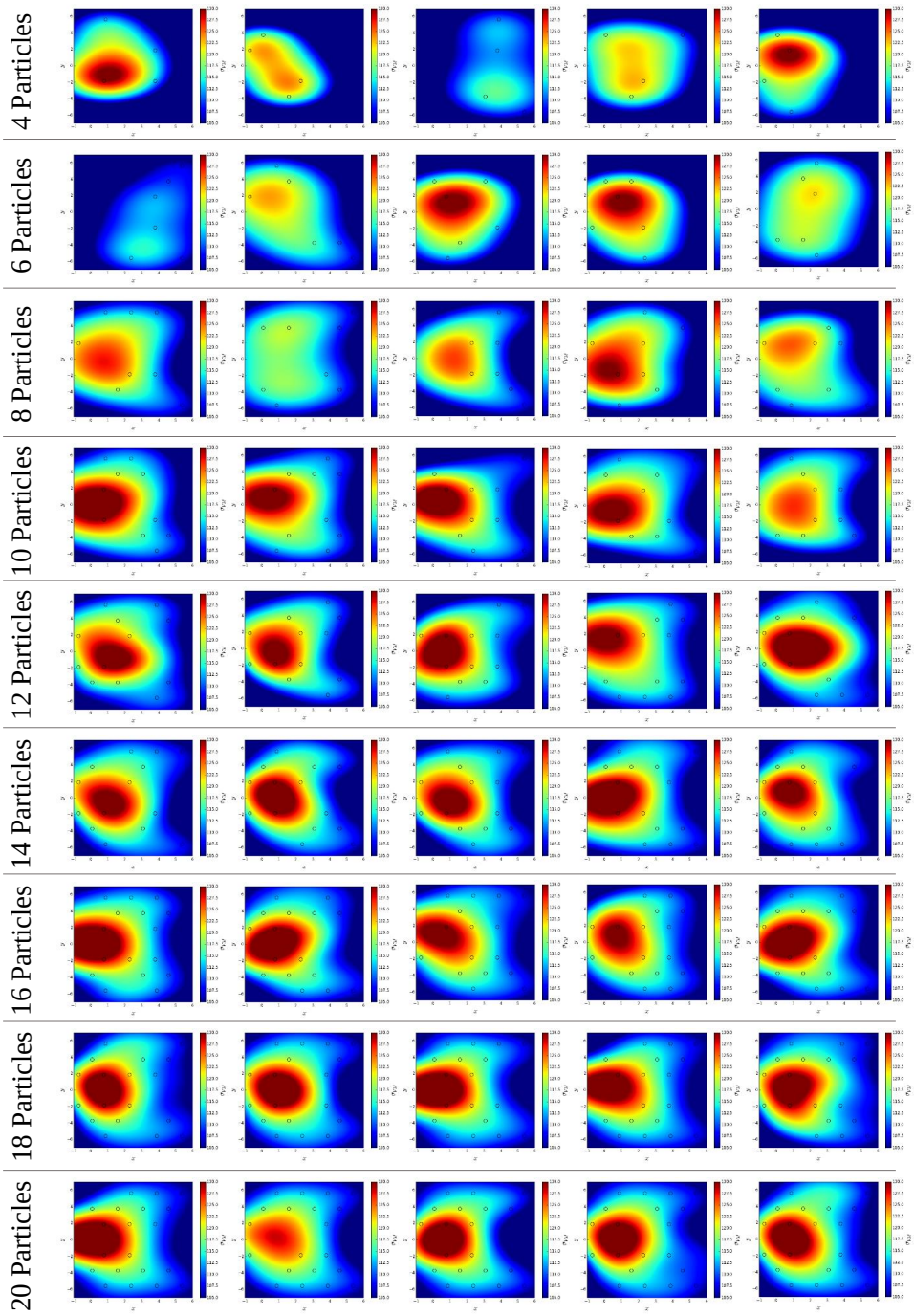

Figure 4.17: Example interpolated stress contour plots for each considered particle density case.

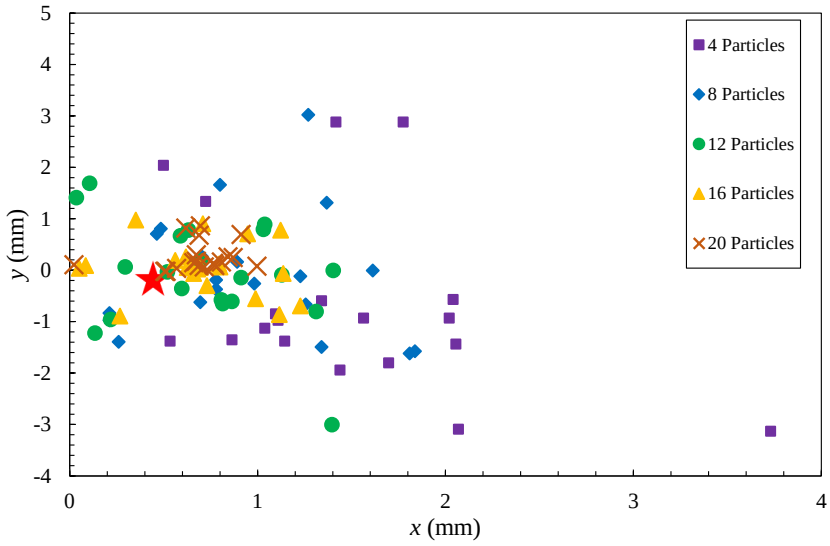

Figure 4.18: Approximated location of the crack tip for each particle configuration. The actual location of the crack tip is denoted by the star.

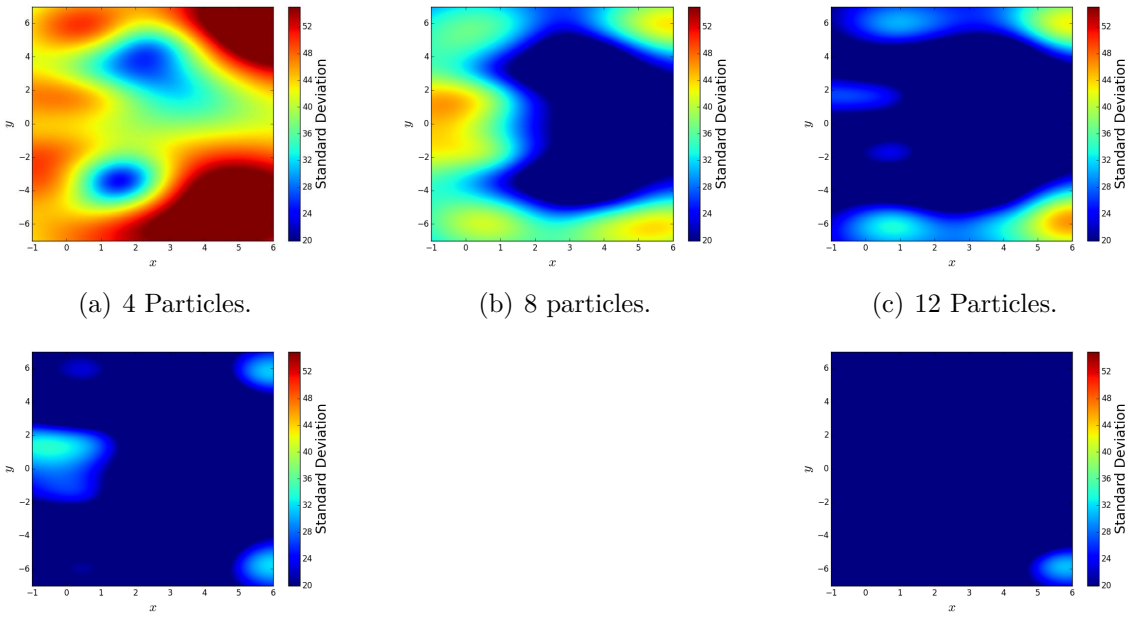

(a) 4 Particles.

(b) 8 particles.

(c) 12 Particles.

(d) 16 Particles.

(e) 20 Particles.

Figure 4.19: Contour plots of the standard deviation of the interpolated stress functions for various particle configurations.

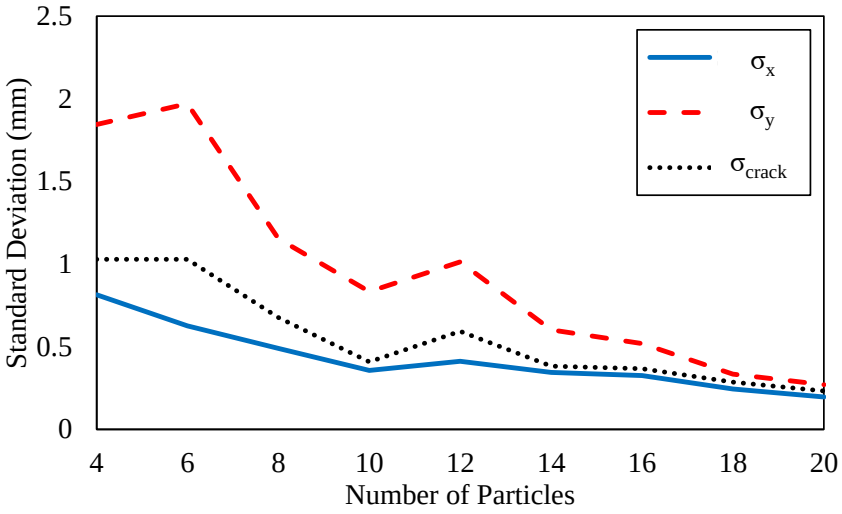

Figure 4.20: Standard deviation in the x-coordinate, y-coordinate, and crack length for each particle configuration.

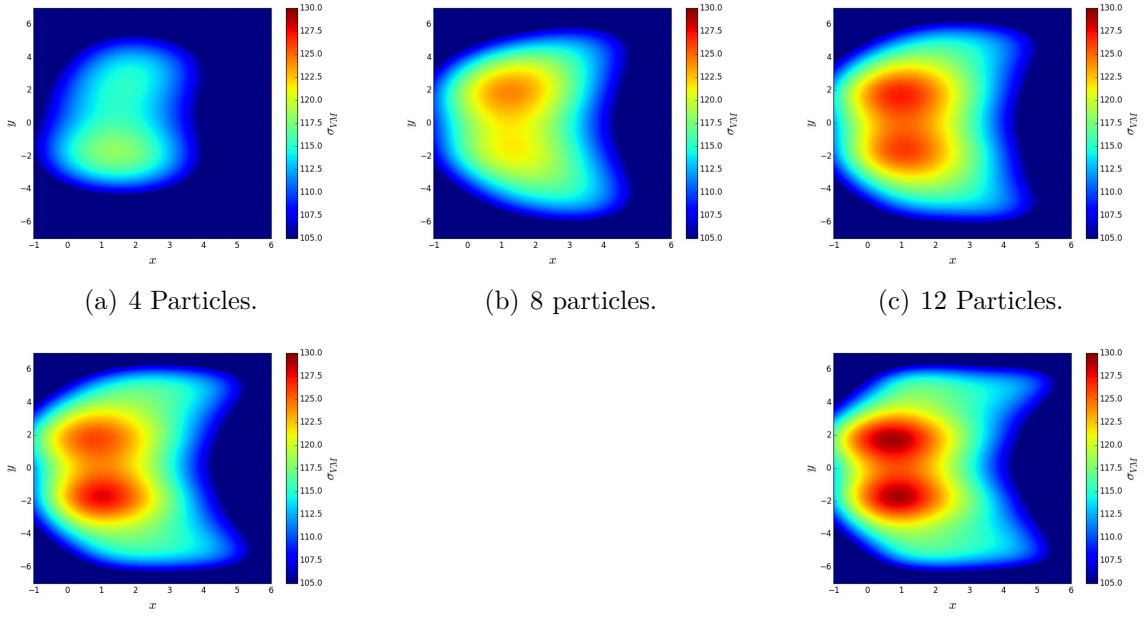

(a) 4 Particles.

(b) 8 particles.

(c) 12 Particles.

(d) 16 Particles.

(e) 20 Particles.

Figure 4.21: Contour plots of the averaged interpolated stress for various particle configurations.

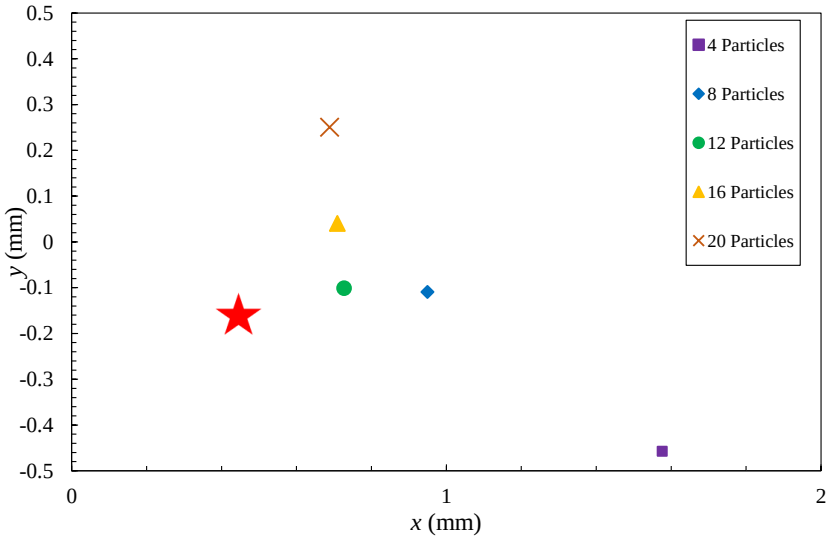

Figure 4.22: Average approximated crack tip location for each particle density configuration. The actual location of the crack tip is denoted by the star.

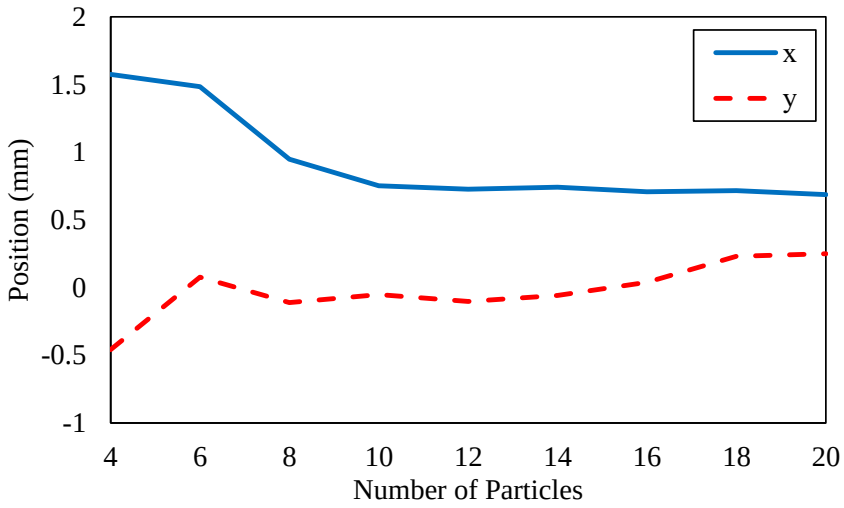

Figure 4.23: Average location of the crack tip for each particle configuration.

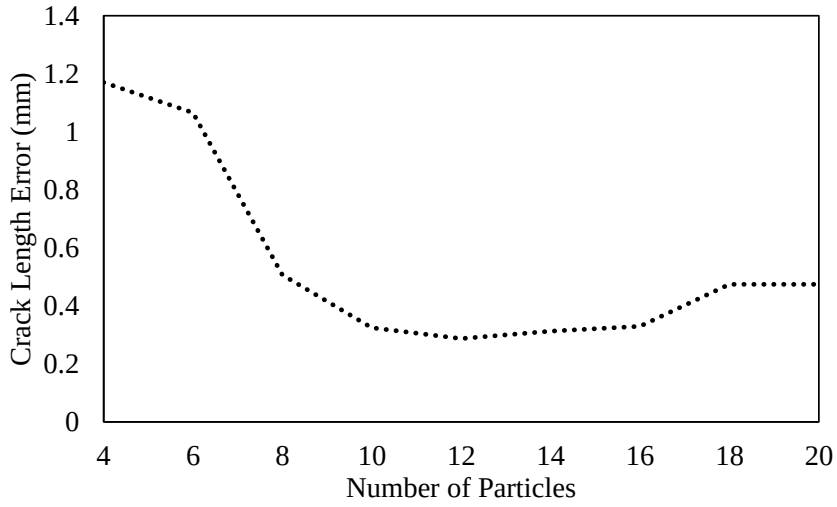

Figure 4.24: Average distance from the actual crack tip for each particle configuration.

5. CONCLUSIONS AND FUTURE WORK

A non-destructive evaluation method for the detection of structural damage that exploits the stress-induced phase transformation behavior of SMA particles has been computationally demonstrated in this work. This method, which would preclude the need for expensive and/or inefficient traditional structural inspection methods, can be combined with smart monitoring systems to provide a near real-time understanding of the integrity of a vehicle's structure. The following sections summarize the findings of this work and offer some ways in which it could be expanded.

5.1 Conclusions

Chapter 2 introduces the experimental and computational methods used in this work. SEM-DIC was utilized to measure the full-field surface deformations of an SMA sensory particle embedded in an aluminum test specimen. These measurements are used to characterize the response of the particle to structural damage. The derivation of the major material models, including the SMA constitutive model, elasto-plastic material model, and a damage model to simulate material degredation, are shown. Methods for efficiently modeling complex structures, modeling crack propagation, and interpolating functions using discrete points are also discussed.

Chapter 3 discusses a method of characterizing local sensory particle response to structural damage. This is necessary due to the altering of SMA material properties during fabrication and processing. This method uses an optimization frame work to minimize the differences between experimental measured strain data and finite element model simulations by changing several material properties. Using a node-release technique to approximate the crack propagation behavior, the optimization framework was able to achieve an acceptable match between experimental and sim-

ulation results. The results of this optimization were then validated using a damage model to simulate a more realistic crack propagation behavior. The inclusion of this damage model resulted in a similar fit between experimental and simulated strain results. Material property trends for developing optimal sensory particles are also discussed. Unlike SMA components for actuation applications, where high transformation strains are desired to produce greater amounts of actuation work, SMA components for sensory applications will generate greater amounts of martensite, and thus a greater magnitude of a detectable response, at lower transformation strains.

Chapter 4 demonstrates the application of the sensory particle method by modeling six embedded particles inside the root rib of a finite element aircraft wing model. As the wing is a complex structure and thus contains hundreds of thousands of elements, substructure modeling is used to maintain the computational viability of the problem. The wingbox and most of the root rib are modeled as substructures, while the portion of the root rib containing the embedded sensory particles is modeled using 3D continuum elements. Two cases were considered: one in which there was no structural damage in the root rib, and one where the particles were embedded in the vicinity of a propagating crack, which was modeled using XFEM. The wing was loaded to 4 G using an assumed elliptical lift distribution, and the responses of each particle in both cases were measured. A comparison of both cases show that particle response is significantly higher when in the vicinity of a propagating crack, confirming the ability of sensory particles to detect structural damage. It was also demonstrated that sensory particle response is independent of surrounding particles. Finally, the effect of particle location relative to the crack tip on particle response was observed, as well as particle response once a crack has propagated past a particle.

Chapter 4 then shifts focus to investigate whether the responses of these sensory particles can be used to not only detect the presence of structural damage, but also

approximate its location. Additionally, the number of particles in the vicinity of a propagating crack to effectively predict the crack tip location is also considered. To this end, the number of particles considered in the finite element model is increased to 24. Particle response at the conclusion of loading is measured for each particle; this response is then related to a given Mises stress value via the SMA constitutive model. RBF interpolation is used to generate a stress contour, where the point of highest stress is considered to be the location of the crack tip. This study consisted of 20 random combinations of n particles to simulate the random dispersion of sensory particles in a component in applications. It was shown that crack tip location predictions became more precise with higher numbers of particles considered, with the most accurate approximation occurring when considering 12 particles. However, the errors associated with each particle configuration considered were well below the critical flaw size, meaning that in most situations all particle configurations can adequately predict the location of a crack tip.

5.2 Future Work

There are several ways in which this work could be extended. First, a new experiment similar to that discussed in Chapter 3 could be performed that accurately records the crack propagation behavior of the specimen. The node-release method used in this work does not take into account the evolution of the interior profile of the crack and thus does not capture the true behavior of the specimen during loading. Another option would be to obtain the data necessary to formulate the damage initiation criterion for the particular aluminum system used. The material properties at the interface of the sensory particles and aluminum matrix were not considered in this work; this interface has a large impact on the forces acting on the sensory particles, and taking this into account would lead to more accurate

simulations of particle response. Additionally, considering more material properties in the optimization framework could lead to a better overall fit to the experimental data.

Chapter 4 could be extended by considering a more complex wing loading. This work assumed an elliptical lift distribution with forces applied to nodes along the main spar; considering a three-dimensional load distribution based on common flight conditions could yield more accurate simulations of the local structural response around the particles and thereby the forces acting on the particles themselves. Additionally, plasticity effects were not considered during crack propagation; particle responses could be altered by the inclusion of such material behavior. It would also be interesting to observe changes in the accuracy of RBF interpolation when considering plasticity.

REFERENCES

[1] Ons Ammar, Nader Haddar, and Luc Remy. Numerical computation of crack growth of low cycle fatigue in the 304L austenitic stainless steel. *Engineering Fracture Mechanics*, 120:67–81, 2014.

[2] BA Auld and JC Moulder. Review of advances in quantitative eddy current nondestructive evaluation. *Journal of Nondestructive evaluation*, 18(1):3–36, 1999.

[3] Ferdinando Auricchio, Robert L Taylor, and Jacob Lubliner. Shape-memory alloys: macromodelling and numerical simulations of the superelastic behavior. *Computer methods in applied mechanics and engineering*, 146(3):281–312, 1997.

[4] Daniel Balageas, Claus-Peter Fritzen, and Alfredo Güemes. *Structural Health Monitoring*, volume 493. Wiley Online Library, 2006.

[5] G Bartelds. Aircraft structural health monitoring, prospects for smart solutions from a European viewpoint. *Structural health monitoring, current status and perspectives*, pages 293–300, 1997.

[6] Ted Belytschko and Tom Black. Elastic crack growth in finite elements with minimal remeshing. *International journal for numerical methods in engineering*, 45(5):601–620, 1999.

[7] D Betz, G Thursby, B Culshaw, and WJ Staszewski. Damage identification using lamb waves and fibre bragg grating sensors. In *Proc. of 2nd Europ. Workshop on Structural Health Monitoring*, pages 1151–1158, 2004.

[8] Daniel C Betz, Graham Thursby, Brian Culshaw, and Wieslaw J Staszewski. Structural damage location with fiber bragg grating rosettes and lamb waves.

Structural health monitoring, 6(4):299–308, 2007.

[9] C Boller, JB Ihn, WJ Staszewski, and H Speckmann. Design principles and inspection techniques for long life endurance of aircraft structures. In *Proc. 3rd Internat. Workshop on Struct. Health Monitoring*, pages 275–283, 2001.

[10] Christian Boller and Matthias Buderath. Fatigue in aerostructuresâĂŤwhere structural health monitoring can contribute to a complex subject. *Philosophical Transactions of the Royal Society of London A: Mathematical, Physical and Engineering Sciences*, 365(1851):561–587, 2007.

[11] Andy P Broeren, Mark G Potapczuk, James T Riley, Philippe Villedieu, Frédéric Moëns, and Michael B Bragg. Swept-wing ice accretion characterization and aerodynamics. *AIAA Paper*, 2824:2013, 2013.

[12] Clifford Bueno, Marion D Barker, Robert A Betz, Richard C Barry, and Robert Buchanan. Nondestructive evaluation of aircraft structures using high-resolution real-time radiography. In *Nondestructive Evaluation of Aging Infrastructure*, pages 114–124. International Society for Optics and Photonics, 1995.

[13] Chatchai Chatwaranon, Sarawan Wongsa, Taywin Buasri, and Anak Khantachawana. Investigation of small electrical resistance of NiTi shape memory alloys in the application of damage detection. In *Electrical Engineering/Electronics, Computer, Telecommunications and Information Technology (ECTI-CON), 2013 10th International Conference on*, pages 1–5. IEEE, 2013.

[14] Yves Chemisky, Rachid Echchorfi, Fodil Meraghni, Nadine Bourgeois, and Boris Piotrowski. Determination of the characteristic parameters of tension-compression asymmetry of shape memory alloys using full-field measurements. In *Materials Science Forum*, volume 738, pages 281–286. Trans Tech Publ, 2013.

[15] Stephen R Cornell, William P Leser, Jacob D Hochhalter, John A Newman, and Darren J Hartl. Development and characterization of embedded sensory particles using multi-scale 3D digital image correlation. In *ASME 2014 Conference on Smart Materials, Adaptive Structures and Intelligent Systems*, pages V002T02A010–V002T02A010. American Society of Mechanical Engineers, 2014.

[16] John E Dennis, Jr and Jorge J Moré. Quasi-Newton methods, motivation and theory. *SIAM review*, 19(1):46–89, 1977.

[17] JD Dougherty, J Padovan, and TS Srivatsan. Fatigue crack propagation and closure behavior of modified 1070 steel: finite element study. *Engineering Fracture Mechanics*, 56(2):189–212, 1997.

[18] I. Dutta, D. Pan, S. Ma, B.S. Majumdar, and S. Harris. Role of shape-memory alloy reinforcements on strain evolution in lead-free solder joints. *Journal of electronic materials*, 35(10):1902–1913, 2006.

[19] John D Eshelby. The determination of the elastic field of an ellipsoidal inclusion, and related problems. In *Proceedings of the Royal Society of London A: Mathematical, Physical and Engineering Sciences*, volume 241, pages 376–396. The Royal Society, 1957.

[20] Charles R Farrar, Scott W Doebling, and David A Nix. Vibration–based structural damage identification. *Philosophical Transactions of the Royal Society of London A: Mathematical, Physical and Engineering Sciences*, 359(1778):131–149, 2001.

[21] Charles R Farrar and Keith Worden. An introduction to structural health monitoring. *Philosophical Transactions of the Royal Society of London A: Mathematical, Physical and Engineering Sciences*, 365(1851):303–315, 2007.

[22] Donald Forney. Nondestructive evaluation technology initiatives program II (NTIP II). delivery order 10, task 010-015: In search of excellence-an historical review. Technical report, DTIC Document, 2006.

[23] EH Glaessgen and David Stargel. The digital twin paradigm for future NASA and US Air Force vehicles. In *53rd Struct. Dyn. Mater. Conf. Special Session: Digital Twin, Honolulu, HI, US*, pages 1–14, 2012.

[24] Wentao He, Jingxi Liu, and De Xie. Numerical study on fatigue crack growth at a web-stiffener of ship structural details by an objected-oriented approach in conjunction with ABAQUS. *Marine Structures*, 35:45–69, 2014.

[25] Sujian Huang. *Continuum theory of plasticity*. John Wiley & Sons, 1995.

[26] W. Huang. On the selection of shape memory alloys for actuators. *Materials & design*, 23(1):11–19, 2002.

[27] David L Hunt, Stanley P Weiss, Walter M West, Terry A Dunlap, and Sam Freesmeyer. Development and implementation of a shuttle modal inspection system. In *International Modal Analysis Conference, 8 th, Kissimmee, FL, Proceedings.*, volume 2, pages 919–925, 1990.

[28] Anthony R. Ingraffea. *Computational Fracture Mechanics*. John Wiley & Sons, Ltd., 2004.

[29] Eric Jones, Travis Oliphant, Pearu Peterson, et al. SciPy: Open source scientific tools for Python, 2001–.

[30] A.D. Kammers and S. Daly. Small-scale patterning methods for digital image correlation under scanning electron microscopy. *Measurement Science and Technology*, 22(12):125501, 2011.

[31] Adam D. Kammers and Samantha Daly. Digital image correlation under scanning electron microscopy: Methodology and validation. *Experimental Mechanics*, 53(9):1743–1761, 2013.

[32] HE Karaca, I Karaman, B Basaran, YI Chumlyakov, and HJ Maier. Magnetic field and stress induced martensite reorientation in NiMnGa ferromagnetic shape memory alloy single crystals. *Acta Materialia*, 54(1):233–245, 2006.

[33] Gaetan KW Kenway, Joaquim RRA Martins, and Graeme J Kennedy. Aerostructural optimization of the common research model configuration. *Group (ADODG)*, 6(7):8–9, 2014.

[34] Kyungmok Kim. High-cycle fatigue simulation for aluminium alloy using cohesive zone law. *Proceedings of the Institution of Mechanical Engineers, Part C: Journal of Mechanical Engineering Science*, page 0954406212454626, 2012.

[35] M. Kimiecik, J.W. Jones, and S. Daly. Quantitative analysis of phase transformation in Ni-Ti shape memory alloys. *Advanced Materials & Processes*, 171(4):21–24, 2013.

[36] Dimitris Lagoudas, Darren Hartl, Yves Chemisky, Luciano Machado, and Peter Popov. Constitutive model for the numerical analysis of phase transformation in polycrystalline shape memory alloys. *International Journal of Plasticity*, 32:155–183, 2012.

[37] Dimitris C Lagoudas. *Shape memory alloys: modeling and engineering applications*. Springer Science & Business Media, 2008.

[38] Weiming Lan, Xiaomin Deng, and Michael A. Sutton. Investigation of crack tunneling in ductile materials. *Engineering Fracture Mechanics*, 77(14):2800–2812, 2010.

[39] Sylvie Legendre, Daniel Massicotte, Jacques Goyette, and Tapan K Bose. Wavelet-transform-based method of analysis for lamb-wave ultrasonic NDE signals. *Instrumentation and Measurement, IEEE Transactions on*, 49(3):524–530, 2000.

[40] WP Leser, JA Newman, JD Hochhalter, VK Gupta, and FG Yuan. Embedded NiTi particles for the detection of fatigue crack growth in aa7050. *Fatigue & Fracture of Engineering Materials & Structures*, 2016.

[41] Ning Li, Siming Guo, and Michael A. Sutton. Recent progress in e-beam lithography for SEM patterning. In *MEMS and Nanotechnology, Volume 2*, pages 163–166. Springer, 2011.

[42] C Louis. Nondestructive testing: radiography, ultrasonics, liquid penetrant, magnetic particle, eddy current. *ASM Int*, 1995.

[43] David G Luenberger. *Introduction to linear and nonlinear programming*, volume 28. Addison-Wesley Reading, MA, 1973.

[44] Howard Matt, Ivan Bartoli, and Francesco Lanza di Scalea. Ultrasonic guided wave monitoring of composite wing skin-to-spar bonded joints in aerospace structures. *The Journal of the Acoustical Society of America*, 118(4):2240–2252, 2005.

[45] Paul E Mix. *Introduction to nondestructive testing: a training guide*. John Wiley & Sons, 2005.

[46] Angela Montoya, Derek Doyle, Arup Maji, and Hans-Peter Dumm. Ultrasonic evaluation of bolted connections in satellites. *Research in Nondestructive Evaluation*, 25(1):44–62, 2014.

[47] Erik Mueller. The detection, inspection, and failure analysis of composite wing skin defects on tactical aircraft. In *24th Advanced Aerospace Materials and Processes (AeroMat) Conference and Exposition*. Asm, 2013.

[48] Hideki Nagai and Ryutaro Oishi. Shape memory alloys as strain sensors in composites. *Smart materials and structures*, 15(2):493, 2006.

[49] NASA. Common Research Model (CRM) wingbox finite element models. On the WWW, March 2014. URL `http://commonresearchmodel.larc.nasa.gov`.

[50] Jorge Nocedal. Updating quasi-newton matrices with limited storage. *Mathematics of computation*, 35(151):773–782, 1980.

[51] Jorge Nocedal and Stephen J. Wright. Numerical optimization 2nd. 2006.

[52] Ryutaro Oishi and Hideki Nagai. Strain sensors of shape memory alloys using acoustic emissions. *Sensors and Actuators A: Physical*, 122(1):39–44, 2005.

[53] M Panico and LC Brinson. A three-dimensional phenomenological model for martensite reorientation in shape memory alloys. *Journal of the Mechanics and Physics of Solids*, 55(11):2491–2511, 2007.

[54] Paul C Paris and George C Sih. Stress analysis of cracks. *Fracture toughness testing and its applications*, pages 30–81, 1965.

[55] Himanshu Pathak, Akhilendra Singh, and Indra Vir Singh. Fatigue crack growth simulations of 3-D problems using XFEM. *International Journal of Mechanical Sciences*, 76:112–131, 2013.

[56] B Peultier, T Ben Zineb, and E Patoor. Macroscopic constitutive law for SMA: Application to structure analysis by FEM. *Materials Science and Engineering: A*, 438:454–458, 2006.

[57] BPC Rao and N Nakagawa. Recommended ndt practice and its model-based investigation for eddy current inspection of aerospace structures. *Journal of Nondestructive Evaluation*, 25(4):183–194, 2006.

[58] Melissa B Rivers and Ashley Dittberner. Experimental investigations of the NASA common research model. *Journal of Aircraft*, 51(4):1183–1193, 2014.

[59] David Roylance. Introduction to fracture mechanics. *Massachusetts Institute of Technology, Cambridge*, 2001.

[60] MW Siegel. Automation for nondestructive inspection of aircraft. 1994.

[61] Petr Šittner, Ludek Heller, Jan Pilch, Caroline Curfs, Thiery Alonso, and Denis Favier. YoungâĂŹs modulus of austenite and martensite phases in superelastic NiTi wires. *Journal of Materials Engineering and Performance*, 23(7):2303–2314, 2014.

[62] Anders Skajaa. Limited memory BFGS for nonsmooth optimization. *Master's thesis, Courant Institute of Mathematical Science, New York University*, 2010.

[63] Henry A Sodano. Development of an automated eddy current structural health monitoring technique with an extended sensing region for corrosion detection. *Structural Health Monitoring*, 6(2):111–119, 2007.

[64] Chellappan Sriram and Ali Haghani. An optimization model for aircraft maintenance scheduling and re-assignment. *Transportation Research Part A: Policy and Practice*, 37(1):29–48, 2003.

[65] WJ Staszewski, S Mahzan, and R Traynor. Health monitoring of aerospace composite structures–active and passive approach. *Composites Science and Technology*, 69(11):1678–1685, 2009.

[66] Y Sumi. Fatigue crack propagation and computational remaining life assessment of ship structures. *Journal of marine science and technology*, 3(2):102–112, 1998.

[67] Guangkai Sun, Zhenggan Zhou, Guanghai Li, and Wenbin Zhou. Development of an optical fiber-guided robotic laser ultrasonic system for aeronautical composite structure testing. *Optik-International Journal for Light and Electron Optics*, 127(12):5135–5140, 2016.

[68] Michael A. Sutton, Ning Li, Dorian Garcia, Nicolas Cornille, Jean Jose Orteu, Stephen R. McNeill, Hubert W. Schreier, and Xiaodong Li. Metrology in a scanning electron microscope: theoretical developments and experimental validation. *Measurement Science and Technology*, 17(10):2613, 2006.

[69] Eric J Tuegel, Anthony R Ingraffea, Thomas G Eason, and S Michael Spottswood. Reengineering aircraft structural life prediction using a digital twin. *International Journal of Aerospace Engineering*, 2011.

[70] John C Vassberg, Mark A DeHaan, S Melissa Rivers, and Richard A Wahls. Development of a common research model for applied CFD validation studies. *AIAA paper*, 6919, 2008.

[71] ABAQUS Version. 6.13. *Analysis User Guide, Dassault Systems*, 2013.

[72] M.M. Abdel Wahab. Simulating mode I fatigue crack propagation in adhesively-bonded composite joints. *Fatigue and Fracture of Adhesively-Bonded Composite Joints*, page 323, 2014.

[73] T.A. Wallace, S.W. Smith, R.S. Piascik, M.R. Horne, P.L. Messick, J.A. Alexa, E.H. Glaessgen, and B.T. Hailer. Strain-detecting composite materials, July 29 2010. US Patent App. 12/685,280.

[74] Andrew P Washabaugh, Vladimir A Zilberstein, Darrell E Schlicker, Ian Shay, David Grundy, and Neil J Goldfine. Shaped-field eddy-current sensors and arrays. In *NDE For Health Monitoring and Diagnostics*, pages 63–75. International Society for Optics and Photonics, 2002.

[75] William Whitten and Darren Hartl. Iterative calibration of a shape memory alloy constitutive model from 1D and 2D experimental data using optimization methods. In *SPIE Smart Structures and Materials+ Nondestructive Evaluation and Health Monitoring*, pages 905804–905804. International Society for Optics and Photonics, 2014.

[76] WE Woodmansee. Aerospace thermal mapping applications of liquid crystals. *Applied optics*, 7(9):1721–1727, 1968.

[77] Shih-Chin Wu and Edward J Haug. Geometric non-linear substructuring for dynamics of flexible mechanical systems. *International Journal for Numerical Methods in Engineering*, 26(10):2211–2226, 1988.

[78] Xiang Zhou, Hans-Peter Gaenser, and Reinhard Pippan. The effect of single overloads in tension and compression on the fatigue crack propagation behaviour of short cracks. *International Journal of Fatigue*, 2016.

APPENDIX A

COMPARISON OF RBF KERNELS FOR STRESS FIELD INTERPOLATION

As mentioned in Section 2.4.2, there are several RBF kernels that can be used for function approximations. Here we consider three such kernels: the mutliquadric form, inverse form, and cubic form. These are given by:

$$\phi(\| \mathbf{x} - \mathbf{x}_i \|) = \sqrt{1 + (\varepsilon \| \mathbf{x} - \mathbf{x}_i \|)^2}, \tag{A.0.1}$$

$$\phi(\| \mathbf{x} - \mathbf{x}_i \|) = \frac{1}{\sqrt{1 + (\varepsilon \| \mathbf{x} - \mathbf{x}_i \|)^2}}, \tag{A.0.2}$$

$$\phi(\| \mathbf{x} - \mathbf{x}_i \|) = \| \mathbf{x} - \mathbf{x}_i \|^3, \tag{A.0.3}$$

where ε is a shape parameter approximated as the average distance between between the given points. Each RBF kernel was used to conduct a particle density study described in Section 4.3.1, where 20 random configurations of n particles were considered. Figure A.1 compares the performance of the three RBF kernels with respect to error and standard deviation in both the x- and y-directions. Notice that, while for high particle densities all three kernels perform approximately the same, both the multiquadric and cubic kernels result in high error and standard deviation at low particle densities; meanwhile, the inverse kernel performs relatively well at low particle densities. Thus, the inverse RBF kernel was chosen for the particle density study.

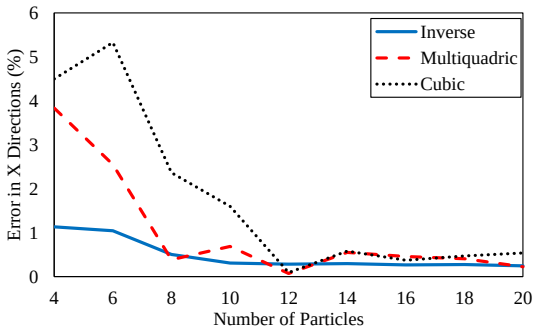

(a) Error in the x-direction.

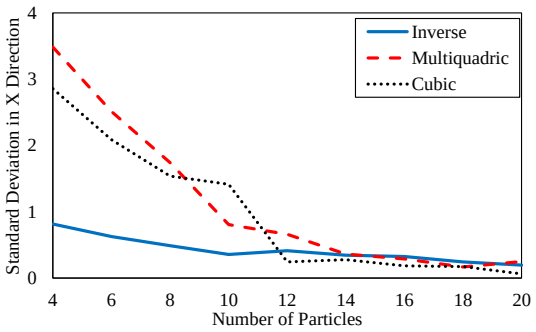

(b) Standard deviation in the x-direction.

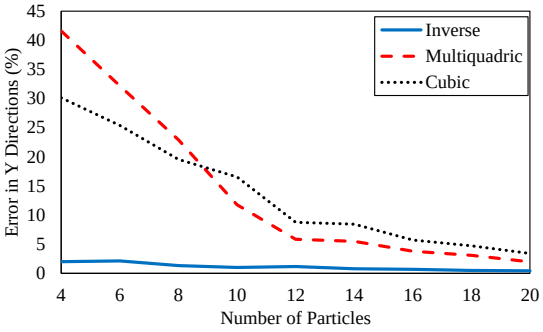

(c) Error in the y-direction.

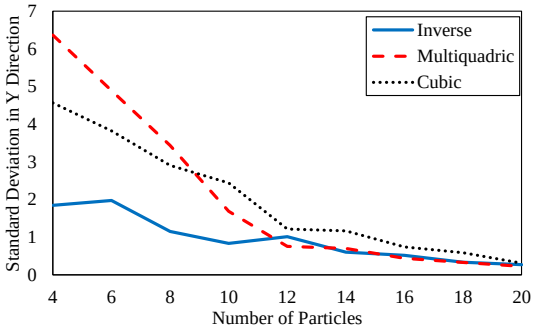

(d) Standard deviation in the y-direction.

Figure A.1: Comparison of three RBF kernels.

APPENDIX B

DERIVATION OF PHASE DIAGRAM PROPERTIES FROM SMA CONSTITUTIVE MODEL

The transformation model parameters $\rho\Delta s_0$, $\rho\Delta u_0$, Y, a_1, and a_3 are defined using phase diagram properties (M_s, M_f, A_s, A_f, C^M, C^A), smooth hardening exponents (n_i, i=1, 2, 3, 4) and the transformation strain (H) as follows [36]:

$$\rho\Delta s_0 = \frac{-2(C^M C^A)(H + \sigma H)}{C^M + C^A}, \tag{B.0.1}$$

$$a_1 = \rho\Delta s_0(M_f - M_s), \tag{B.0.2}$$

$$a_2 = \rho\Delta s_0(A_s - A_f), \tag{B.0.3}$$

$$a_3 = -\frac{a_1}{4}\left(1 + \frac{1}{n_1 + 1} - \frac{1}{n_2 + 1}\right) + \frac{a_2}{4}\left(1 + \frac{1}{n_3 + 1} - \frac{1}{n_4 + 1}\right), \tag{B.0.4}$$

$$\rho\Delta u_0 = \frac{\rho\Delta s_0}{2}(M_s + A_f), \tag{B.0.5}$$

$$Y = \frac{\rho\Delta s_0}{2}(M_s - A_f) - a_3. \tag{B.0.6}$$

APPENDIX C

TABLE LOOK-UP FOR DAMAGE MODEL

Table C.1: Table associated with the equivalent plastic strain $\bar{\varepsilon}_D^{pl}$ for a given stress triaxiality η and plastic strain rate $\dot{\bar{\varepsilon}}^{pl}$, as discussed in Section 3.4.

$\bar{\varepsilon}_D^{pl}$	η	$\dot{\bar{\varepsilon}}^{pl}$	$\bar{\varepsilon}_D^{pl}$	η	$\dot{\bar{\varepsilon}}^{pl}$
208	-3.33	0.001	465.088	-3.33	250
207.971	-0.333	0.001	465.088	-0.333	250
118.795	-0.267	0.001	250.192	-0.267	250
67.8571	-0.2	0.001	134.589	-0.2	250
38.7612	-0.133	0.001	72.4019	-0.133	250
22.1419	-0.0667	0.001	38.9487	-0.0667	250
12.6496	0	0.001	20.9533	0	250
7.229	0.0667	0.001	11.2736	0.0667	250
4.1354	0.133	0.001	6.068	0.133	250
2.3728	0.2	0.001	3.2707	0.2	250
1.3739	0.267	0.001	1.7715	0.267	250
0.8173	0.333	0.001	0.9753	0.333	250
0.5237	0.4	0.001	0.5662	0.4	250
0.3988	0.467	0.001	0.3817	0.467	250
0.4021	0.533	0.001	0.3488	0.533	250
0.535	0.6	0.001	0.4542	0.6	250
0.84	0.667	0.001	0.74	0.667	250
0.5008	0.73	0.001	0.4193	0.73	250
0.187	0.851	0.001	0.1421	0.851	250
0.0457	1.02	0.001	0.0302	1.02	250
0.0076	1.24	0.001	0.0042	1.24	250
0.0001	1.51	0.001	0.0001	1.51	250
0.0001	3.33	0.001	0.0001	3.33	250